Naval Research Laboratory
Washington, DC 20375-5320

NRL/MR/8120--97-7971

Analysis of SLR Targets for JASON

G. Charmaine Gilbreath
Peter B. Rolsma
Robert Kessel

Advanced Systems Technology Branch
Space Systems Development Department

September 30, 1997

19971016 156

REPORT DOCUMENTATION PAGE

Form Approved
OMB No. 0704-0188

1. AGENCY USE ONLY *(Leave Blank)*	2. REPORT DATE September 30, 1997	3. REPORT TYPE AND DATES COVERED Final Report

4. TITLE AND SUBTITLE Analysis of SLR Targets for JASON	5. FUNDING NUMBERS
6. AUTHOR(S) G. Charmaine Gilbreath, Peter B. Rolsma, and Robert Kessel	
7. PERFORMING ORGANIZATION NAME(S) AND ADDRESS(ES) Naval Research Laboratory Washington, DC 20375-5320	8. PERFORMING ORGANIZATION REPORT NUMBER NRL/MR/8120--97-7971
9. SPONSORING/MONITORING AGENCY NAME(S) AND ADDRESS(ES) Jet Propulsion Laboratory 4800 Oak Grove Drive Pasadena, California 91109	10. SPONSORING/MONITORING AGENCY REPORT NUMBER
11. SUPPLEMENTARY NOTES	
12a. DISTRIBUTION/AVAILABILITY STATEMENT Approved for public release; distribution unlimited.	12b. DISTRIBUTION CODE

13. ABSTRACT *(Maximum 200 words)*

This report provides preliminary results pertaining to the applicability to the JASON program of a retroreflector array designed, built, and space qualified by the Naval Research Laboratory for Low Earth Orbiting spacecraft. In this report, we will describe the assumptions we used for link analysis as they pertain to Passes 44 and 85 over Capraia Island. We provide figures and discussions pertinent to a single retroreflector's performance and the array's performance over the site. We also include a description and photo of the array itself, as well as the test and levels used to space qualify the array.

14. SUBJECT TERMS Satellite laser ranging SLR Retroreflectors	Retrorelector Orbit determination	15. NUMBER OF PAGES 53
		16. PRICE CODE

17. SECURITY CLASSIFICATION OF REPORT UNCLASSIFIED	18. SECURITY CLASSIFICATION OF THIS PAGE UNCLASSIFIED	19. SECURITY CLASSIFICATION OF ABSTRACT UNCLASSIFIED	20. LIMITATION OF ABSTRACT UL

NSN 7540-01-280-5500

Standard Form 298 (Rev. 2-89)
Prescribed by ANSI Std 239-18
298-102

CONTENTS

FIGURES

ANALYSIS OF SLR TARGETS FOR JASON

1 INTRODUCTION

This report presents an analysis of a design for a retroreflector array for the JASON spacecraft and mission. The analysis includes the direct numerical computation of a single retroreflector's and array's optical properties as well as the space qualification characterization of the array's mechanical properties. The purpose of the array is to provide maximized cross section return for the Field Transportable Laser Radar Station (FTLRS) telescope on the island of Capraia Island.

Satellite Laser Ranging (SLR) data is an extremely powerful tool for precise orbit determination. Direct detection SLR provides position estimation comparable with differential GPS and is used as the referenced "truth" by the scientific community for geoscience and navigation. Although SLR data serves as a high precision orbit estimator, it is weather dependent. Therefore, this data type is uniquely suited for independent system performance validation of onboard spacecraft systems and periodic calibration.

The report opens with a review of SLR systems establishing both general terminology and specific assumptions relevant to JASON in Section 2. Section 3 considers single retroreflectors and Section 4 discusses the analysis of the retroreflector array. Core results from the space qualification testing of the retroreflector array are summarized in Section 5.

Manuscript approved August 29, 1997

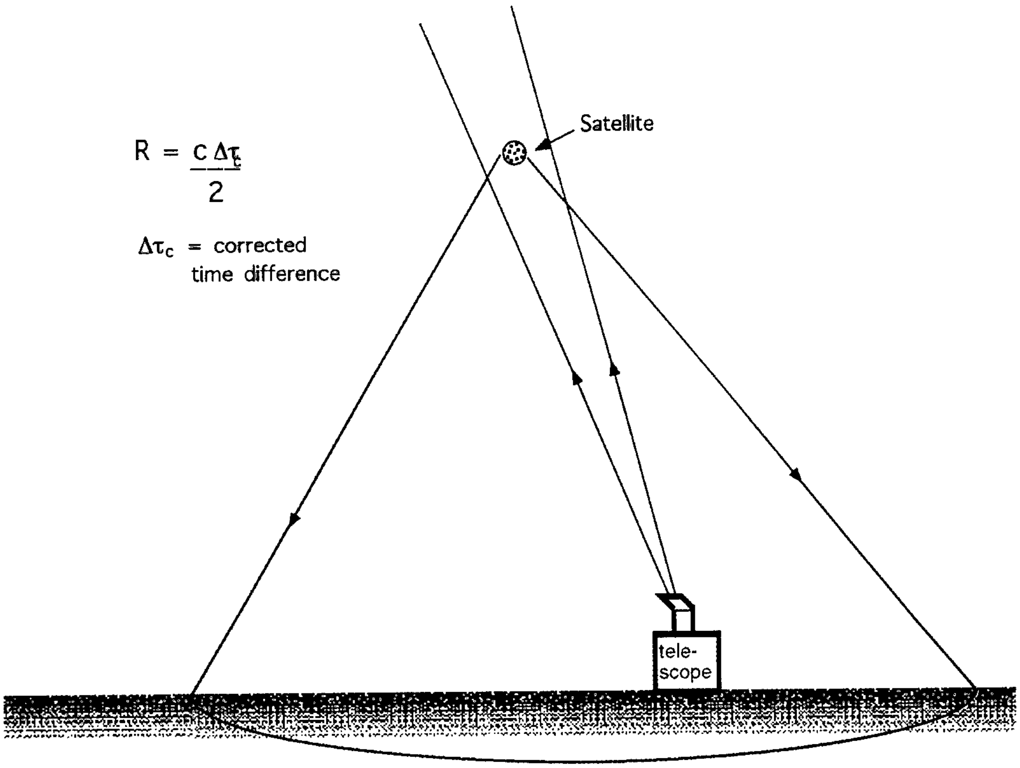

Figure 1: Schematic diagram of Satellite Laser Ranging.

2 SATELLITE LASER RANGING SYSTEM CHARACTERISTICS

Satellite Laser Ranging in the context of this report is direct-detection radar in the optical wavelength regime. When an orbit is properly sampled and the SLR data acquisition system is properly configured and calibrated, residuals and accuracies on the order of centimeters are routinely obtained using this method.

Figure 1 illustrates the basic aspects of the technique. Time-tagged time-of-flight differences are recorded, corrected for system delays, and converted to ranges. These ranges then provide input to an orbit determination model which is used to generate the three dimensional estimate of the spacecraft's orbit and position.

2.1 Return Pulse Detection and System Trade-offs

As discussed in Degnan's review [1], the number of photoelectrons generated by the return pulse detection is given by the laser radar link equation

$$N_{\mathrm{pe}} = \eta_D E_0 \left(\frac{\lambda}{hc}\right) \eta_T G_T \sigma_{\mathrm{LRCS}} \left(\frac{1}{4\pi R^2}\right)^2 A_R \eta_R T_a^2 T_c^2 \quad . \tag{1}$$

The factors in Equation 1 are:

η_D	Detector Quantum Efficiency	σ_{LRCS}	Laser Radar Cross Section
E_0	Transmit Energy	R	Slant Range
λ	Wavelength	A_R	Receiver Telescope Area
h	Planck's Constant	η_R	Receiver Efficiency
c	Speed of Light	T_a	One-way Atmospheric Transmission
η_T	Transmission Efficiency	T_c	One-way Cirrus Cloud Transmission
G_T	Transmitter Gain		

In cases where the system figure of merit is the number of return pulse photons reaching the front aperture of the receive telescope, $N_{\gamma,\text{tele}}$, then

$$\begin{aligned} N_{\gamma,\text{tele}} &= \frac{N_{\text{pe}}}{\eta_R \eta_D} \\ &= E_0 \left(\frac{\lambda}{hc}\right) \eta_T G_T \sigma_{\text{LRCS}} \left(\frac{1}{4\pi R^2}\right)^2 A_R T_a^2 T_c^2 \quad . \end{aligned} \tag{2}$$

Equation 2 is an absolute number of photons and depends on the telescope aperture A_R. If the photon flux itself is needed for ground station trade studies, it is given by

$$\text{flux}_\gamma = \frac{N_{\text{pe}}}{A_R \eta_R \eta_D} \quad . \tag{3}$$

Since the JASON Specification in Section 2.2 use a fixed ground station, the results of this report are given in terms of N_{pe} and $N_{\gamma,\text{tele}}$ for a 13 cm aperture only.

The factors in Equation 1 determine the SLR trade-space and can be grouped four categories: transfer efficiencies, transmitted pulse magnitude, environmental/orbit parameters, and geometric factors. The three transfer efficiencies, η_D, η_T, and η_R, are fixed by the technology of the ground station. The initial number of photons, $E_0\left(\frac{\lambda}{hc}\right)$, is determined by the laser source. Three of the remaining factors in Equation 1 are environmental parameters determined by the satellite's orbit and the specific ground station location and time of the measurement (*i.e.* R, T_a, or T_c). These environmental/orbital parameters are beyond the experimenters' control. Two of the geometric factors, G_T and A_R, are associated with transmitting and receiving the laser ranging pulse at the ground station. Assuming Gaussian beam profile, the transmitter gain is

$$G_T = \left(\frac{8}{\theta_T^2}\right) e^{-2(\theta_{\text{point}}/\theta_T)^2} \quad , \tag{4}$$

where θ_T is the divergence half-angle and θ_{point} is the pointing uncertainty. The remaining geometric factor, σ_{LRCS}, is determined by the SLR target and will be a primary focus of this report's analyses. An extended treatment of each of the parameters in Equation 1 is given in Degnan [1].

2.2 JASON System Specifications and Orbit Characteristics

For this analysis, we assumed a typical TOPEX/POSEIDAN orbit: nominally circular, with 66.0° inclination, and an altitude over the site of 1,330 km. The site itself was assumed to be Capraia Island, latitude: 43°0′ N; longitude: 9°45′ E. The expected performance of the single retroreflector and the 22 element array was determined for Passes 44 and 85 over this location.

For the link analysis, we assumed that the transmit/receive (T/R) system has the following characteristics: Wavelength: 532 nm and 1064 nm; Average Energy: 100 mJ; Pulse width: 100 ps at 532 nm; Transmission Path Efficiency: 50%; Telescope Diameter: 13 cm; and Beam Divergence (Full angle): 100 μrad. We used MODTRAN to estimate the atmospheric transmission T_a for

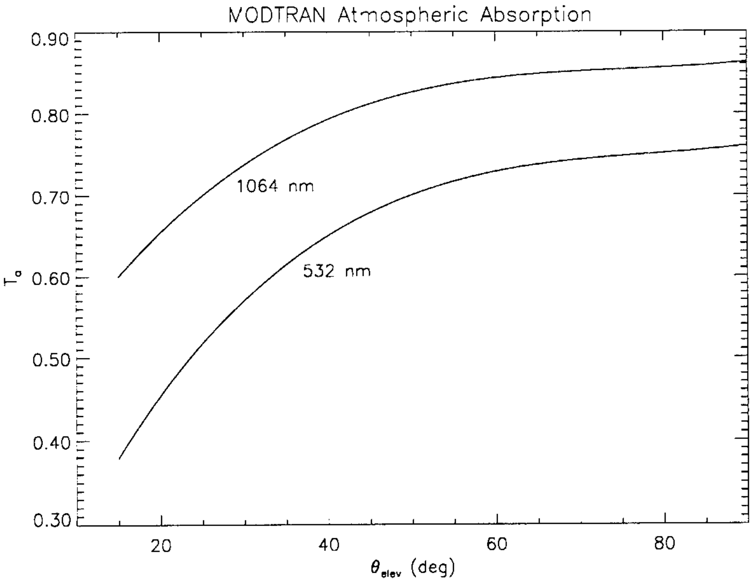

Figure 2: MODTRAN estimates for atmospheric transmission T_a as a function of elevation angle θ_{elev} for a clear sky at 532 nm and 1064 nm above Capraia Island.

Capraia Island. The atmospheric transmission is shown as a function of elevation angle in Figure 2 for both 532 nm and 1064 nm. We assumed that no cirrus clouds were present and, hence, $T_c = 1$.

The system pointing uncertainty was unspecified, so we analyzed the link for two different values of this parameter. Based on our experience on the NRL@SOR mount [2] where pointing jitter was on the order of an arcsecond (4.85μrad), we estimated jitter to be on the order of 2 arcsec for the analysis in one case. We also analyzed the array's performance based on the tracking uncertainty of the 1988 Transportable Laser Ranging System (TLRS) upgrade, which is estimated to be 5.4 arcsec. As will be seen in the results, the difference in these two levels of uncertainty impact the predicted photoelectron and photon returns.

The JASON specification stated that the design shall provide a return power of 100 photons using a Receiver efficiency of 20% in the green and 2–4% in the infrared, where these percentages reflect the combined receive path and detector efficiencies. If, in fact, that is the case, then we were provided with the effective receiver efficiencies to produce the number of photoelectrons, not photons. The detector efficiency is the conversion efficiency from photons to photoelectrons. Therefore, we analyzed the performance of the array in terms of photoelectrons, N_{pe}, using 20% for 532 nm and 4% for 1064 nm. However, we also provide photons received at the telescope, $N_{\gamma,\mathrm{tele}}$, for an assumed 13 cm diameter aperture. These numbers can be converted by the product of the receiver path efficiency and detector efficiency, $\eta_R \eta_D$, to the number of detected photoelectrons.

2.3 Target Diffraction Effects and σ_{LRCS}

The typical target for an SLR application uses one or more retroreflectors. A cube corner retroreflector (or cube for short) is made of three mutually perpendicular reflective flats. The configuration returns light along the path of incidence, and therefore, avoids a requirement for precise orientation of the target with respect to the ground site. However, since the retroreflector's aperture is of finite size, the reflected light is spread by diffraction. The transmitted pulse travels hundreds of kilometers and over the retroreflector's aperture the wave fronts are indistinguishable from a plane wave. When combined with the return path, the geometry satisfies the Fraunhofer limit. Consequently, the return pulse spatial distribution is the aperture's Far Field Diffraction Pattern (FFDP). Further, the FFDP follows standard diffraction scaling in which a smaller aperture retroreflector generates a broader FFDP. The FFDP's breadth is of particular importance since, in combination with the satellite velocity aberration, it plays a significant role in overall SLR system performance.

In Equation 1 the SLR target's diffraction characteristics are carried by the laser radar cross section, σ_{LRCS}. Denoting the FFDP by $\tilde{a}(k_x, k_y)$, the relationship between the two quantities is

$$\sigma_{\mathrm{LRCS}}(k_x, k_y) = \frac{4\pi}{\lambda^2}|\tilde{a}(k_x, k_y)|^2 \tag{5}$$

(see Minott, [3] [4]) where,

$$k_x = \frac{2\pi}{\lambda}\sin\theta_x \tag{6}$$

and

$$k_y = \frac{2\pi}{\lambda}\sin\theta_y \quad . \tag{7}$$

The angles θ_x and θ_y define the observation direction. If an FFDP is observed at x_o and y_o from a range R, then $\sin\theta_x = x_o/R$ and $\sin\theta_y = y_o/R$ respectively. One is equally free to use a position and a distance, but for general work it is more convenient to use angles. The results of this report are given in terms of angular measure. Equation 5 assumes perfect reflectivity. A more realistic description of a real retroreflector is

$$\sigma_{\mathrm{LRCS}}(k_x, k_y) = \rho\frac{4\pi}{\lambda^2}|\tilde{a}(k_x, k_y)|^2 \quad , \tag{8}$$

where ρ is a reflectivity. In the computations supporting this report, $\rho = 0.75$ which is a conservative estimate including manufacturing errors as well the reflectivity loss itself.

2.4 Satellite Velocity Aberration

Because the satellite is moving with respect to the ground station, the part of the intensity distribution from the return pulse which is observed at the ground station is offset with respect to the central maximum of the diffraction pattern. This offset is called the satellite velocity aberration or Bradley effect [3]. Figure 3 shows schematically the combined effects of the diffracted return pulse and the velocity aberration. The velocity aberration expressed as a displacement vector in the far field diffraction pattern (or σ_{LRCS}) is given by

$$\vec{\mathbf{k}} = \left(\frac{2\pi}{\lambda}\right)\left(\frac{2\vec{\mathbf{v}}_\perp}{c}\right) \quad , \tag{9}$$

where $\vec{\mathbf{v}}_\perp$ is the satellite's apparent perpendicular velocity. The displacement vector $\vec{\mathbf{k}}$ selects which value of the instantaneous σ_{LRCS} from Equation 8 is used in Equation 1 at each point in time during a satellite's pass over a ground station.

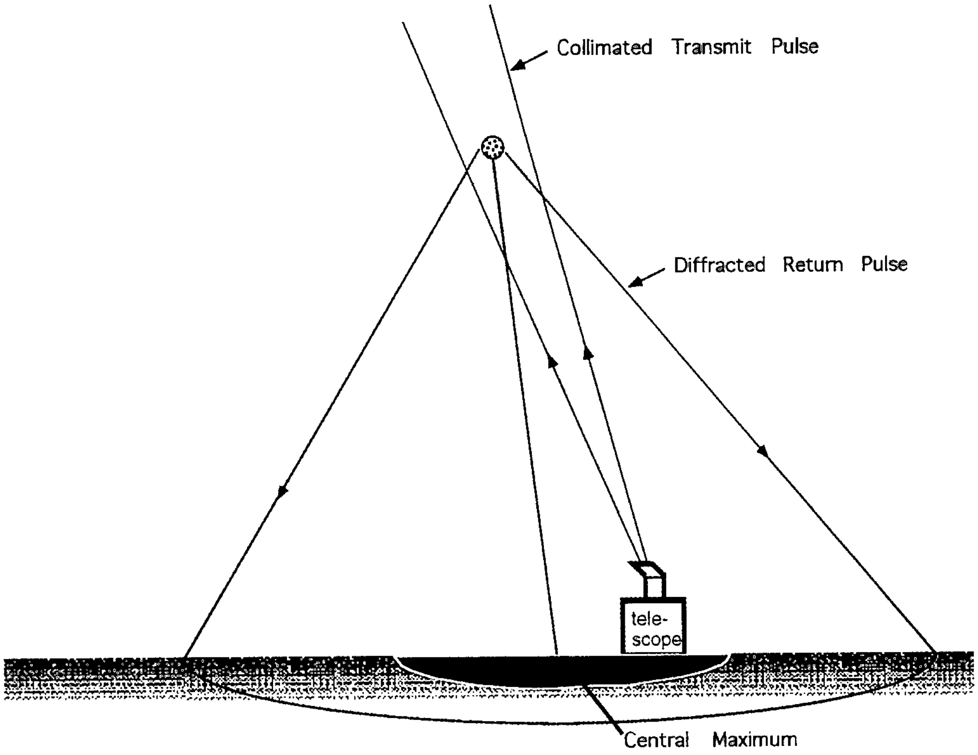

Figure 3: The SLR target size determines the spatial distribution of the diffracted return pulse. The satellite's apparent orbital velocity determines offset between the central maximum of the diffraction pattern and the ground station.

3 SATELLITE LASER RANGING WITH SINGLE RETROREFLECTOR TARGETS

This section discusses the received signal strength from a single retroreflector on a satellite. The section first covers the results from our numerical computation of σ_{LRCS} for four cases beginning with the highest symmetry: 1. normal incidence without bevels, 2. tilted incidence without bevels, 3. normal incidence with bevels, and 4. tilted incidence with bevels. Each case serves as a limit test case for the numerical routines of the succeeding cases. The second part of the section discusses the combination of the σ_{LRCS} values with rest of the SLR system to predict system performance.

3.1 Circular Retroreflector Far Field Diffraction Patterns and Laser Radar Cross Sections

3.1.1 Normal Incidence

When a plane wave pulse hits the retroreflector, it is exactly reversed in direction along the path of incidence. As discussed in Section 2.3, the retroreflector's finite aperture modifies the incidence plane wave pulse and returns a diffracted pulse. At the ground station the return pulse has the spatial distribution of the aperture's far field diffraction pattern. A single circular retroreflector without bevel losses observed at normal incidence provides a geometry with sufficiently high symmetry that an analytic expression exists for the FFDP. The FFDP is the Airy function (Born and Wolfe, [5]; Goodman, [6]), and hence,

$$\sigma_{\text{LRCS}}(k) = \frac{4\pi A^2}{\lambda^2}\left(\frac{2J_1(rk)}{rk}\right)^2 \quad , \tag{10}$$

where A is the area of the retroreflector, r is the retroreflector radius, and

$$k = \frac{2\pi}{\lambda}\sin\theta \quad . \tag{11}$$

At normal incidence, σ_{LRCS} has azimuthal symmetry and Equation 10 is a function of the single magnitude variable k only.

Figure 4 shows σ_{LRCS} as function of k (a radial slice in k_x, k_y) for 2.54 cm and 1 cm aperture sizes. While both curves were computed numerically with the FFDP routines described in Section A.1, they agree with Equation 10 to machine precision. The correct geometry required for a normal incidence observation can occur only when the satellite is directly above the ground station and the retroreflector normal is aligned with the nadir direction. The velocity aberration for a 1,330 km circular orbit at zenith is approximately k of 50 μradians. Thus, as can be seen in Figure 4, although σ_{LRCS} for the 2.54 cm retroreflector is significantly larger at $k = 0$, the broader FFDP of the 1 cm retroreflector has an equivalent σ_{LRCS} at k of 50 μradians and greater constancy (less variation) throughout the pattern. Figure 5 shows a contour plot of σ_{LRCS} of a 1 cm circular retroreflector as a function of k_x and k_y. Note that the velocity aberration given by Equation 9 selects a single k_x, k_y point in Figure 5 for which the σ_{LRCS} value would be used in Equation 1.

3.1.2 Off-axis Incidence

At all other points in an orbital pass, the retroreflector tips away from normal incidence, so its projected aperture changes in shape and decreases in area. Figure 6 shows how both the shape of the projected aperture and area changes as a function of incidence angle θ_{inci}. Note that the projected aperture decreases in size along both axes. The decrease in projected aperture size increases the

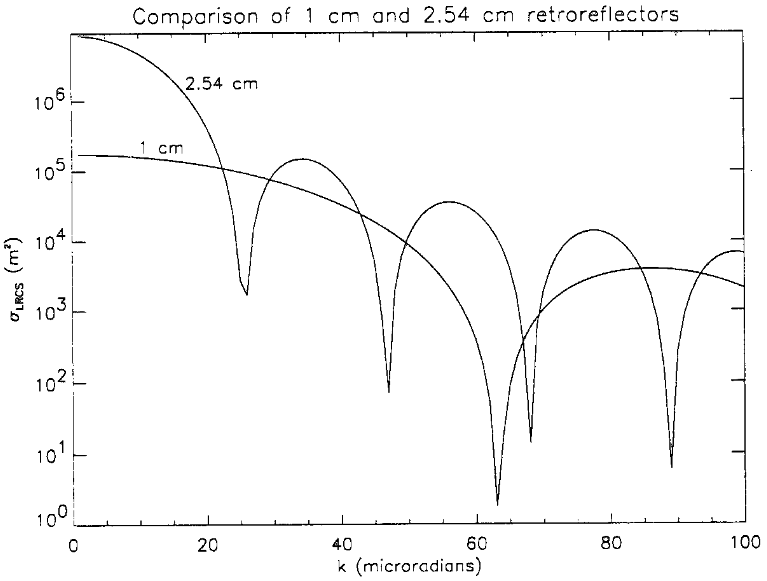

Figure 4: σ_{LRCS} at normal incidence for a 2.54 cm (1″) and 1 cm circular retroreflectors as a function of k.

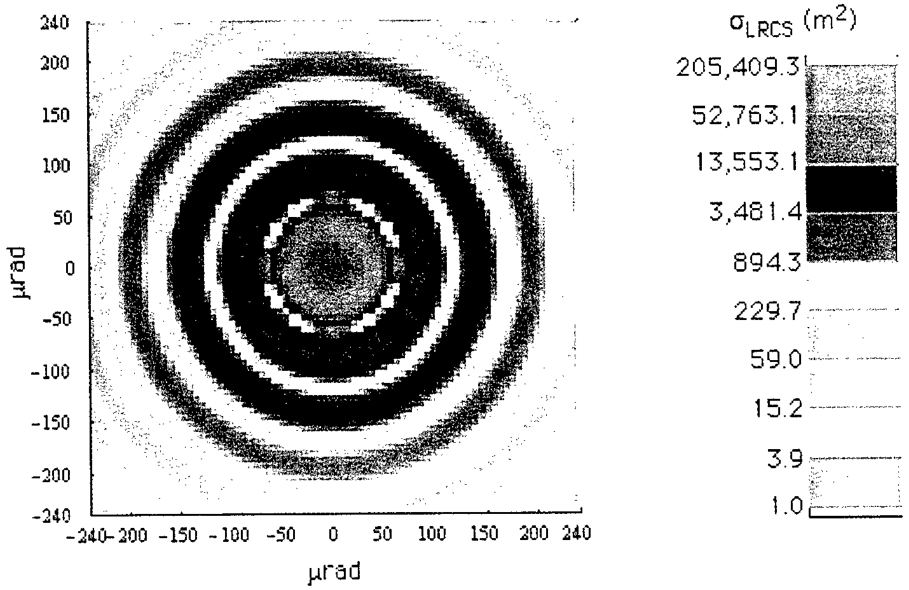

Figure 5: Plot of σ_{LRCS} at normal incidence for a 1 cm circular retroreflector without bevels as a function of k_x and k_y given in terms of μradians.

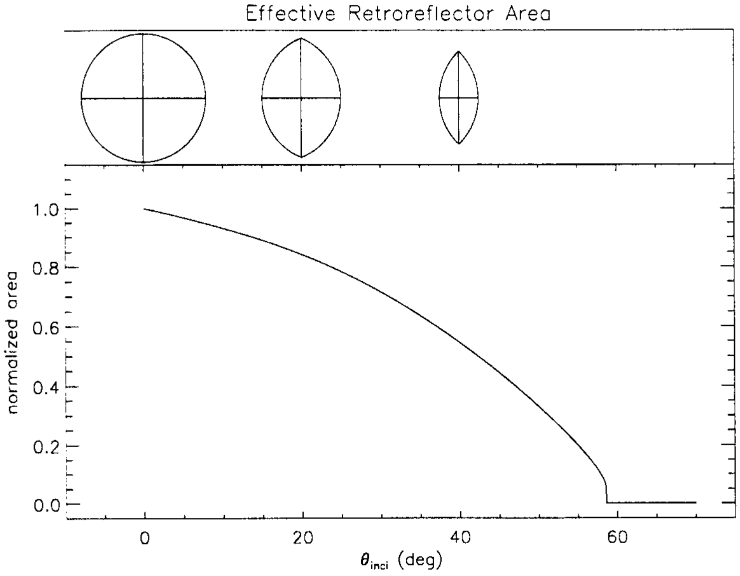

Figure 6: Top Panel: Retroreflector Aperture Shape: 1. Normal incidence, 2. 20° from normal incidence, 3. 40° from normal incidence. Bottom Panel: The normalized retroreflector aperture area as a function of incidence angle θ_{inci}.

angular extent of the FFDP proportionally and decreases its overall magnitude. The change in aperture shape eliminates azimuthal symmetry so an analytic closed form expression for the FFDP (*e.g.* Airy function) is no longer possible. Appendix A.1 describes a method to numerically compute the FFDP.

Figure 7 shows $\sigma_{\rm LRCS}$ of a tilted 1 cm circular retroreflector computed numerically without bevel losses. The azimuthal symmetry present for normal incidence has been reduced to a two-fold rotational symmetry as seen from the ellipticity of the contours. The central maximum around $k_x = k_y = 0$ remains smoothly rounded. However, there is a sizable variation in $\sigma_{\rm LRCS}$ as one holds the magnitude of $\vec{\rm k}$ fixed and sweeps around in k_x, k_y. Physically this corresponds to holding the retroreflector axis at a fixed tilt while sweeping the observation direction around at a fixed angle. This variation is shown in Figure 8 for a 10° tilt from normal incidence and $|\vec{\rm k}|$ of 50 μradians as a function of observation direction angle.

3.1.3 Bevel Losses

Beveled edges are required at the reflecting face plane intersections during the polishing of real retroreflector cubes. Adding bevels introduces narrow loss regions within the aperture. More general versions of our numerical simulations include these losses in both normal incidence or off-axis cases (Sections A.1.3 and A.1.4). At normal incidence, the three bevel loss regions and their reflections generate a six-fold rotation symmetry in diffraction pattern and $\sigma_{\rm LRCS}$. Since the bevels are relatively narrow, the six-fold symmetry is more pronounced at larger values of $|\vec{\rm k}|$ beyond the first diffraction minimum. Figure 9 shows $\sigma_{\rm LRCS}$ at normal incidence of circular retroreflector computed numerically with losses from 0.008″ bevels. The variation in $\sigma_{\rm LRCS}$ as one sweeps around in k_x, k_y is shown in Figure 10 for 0.008″ bevels at $|\vec{\rm k}|$ of 50μradians

As can be seen from the comparison of Figures 8 and 10, the effect of tilting the retroreflector is much more significant than adding the bevels. While our numerical computation treats the bevel's

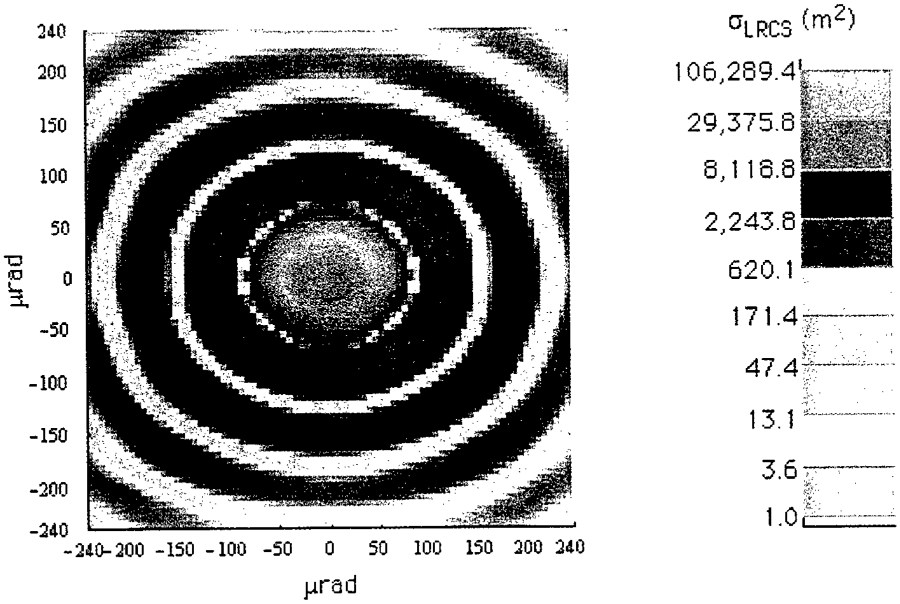

Figure 7: Plot of σ_{LRCS} of a 1 cm circular retroreflector as a function of k_x and k_y given in terms of μradians, with 10° tilt. Ellipticity of the contours is the result.

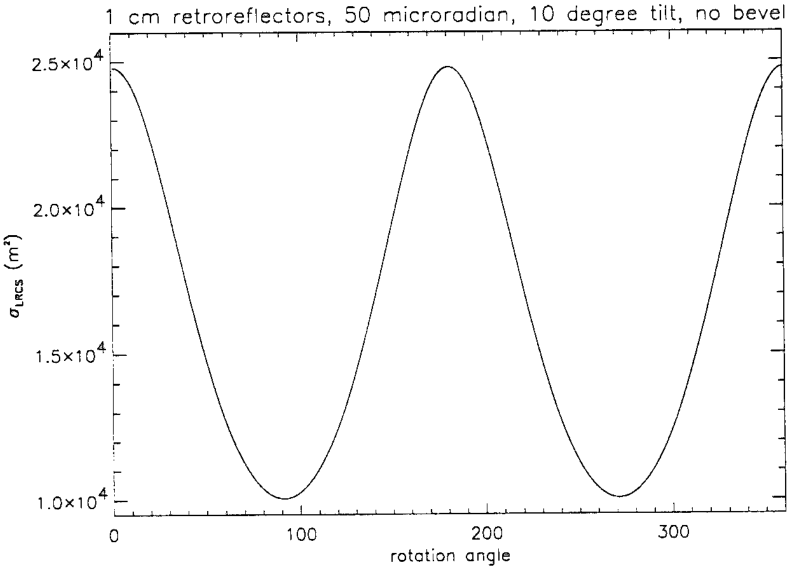

Figure 8: Variation in σ_{LRCS} at 10° off-axis from normal incidence of a 1 cm circular retroreflector at $|\vec{\mathbf{k}}|$ of 50 μradians. The variation in σ_{LRCS} from its average caused by a fixed 10° tilt by a rotation of the observation direction is 42%. At the instant of pulse reflection, a satellite's apparent perpendicular velocity determines the observation direction.

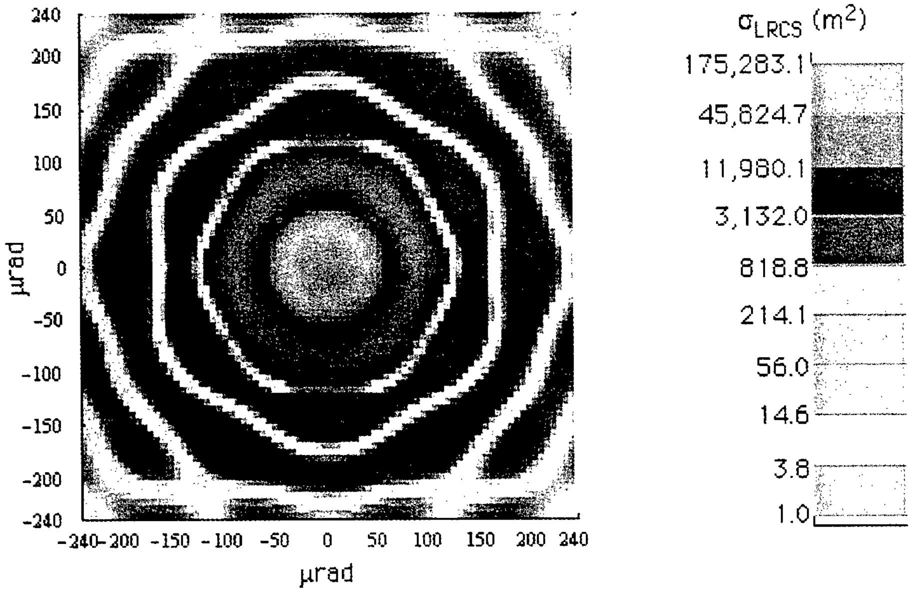

Figure 9: Plot of σ_{LRCS} of a 1 cm circular retroreflector with 0.02032 cm (or 0.008″) bevels as a function of k_x and k_y given in terms of μradians for normal incidence.

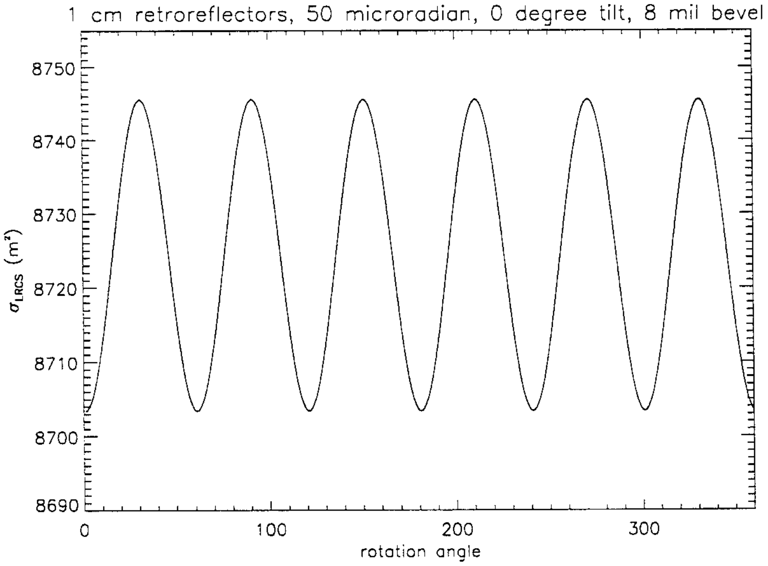

Figure 10: The variation in σ_{LRCS} at normal incidence of a 1 cm circular retroreflector at $|\vec{\mathbf{k}}|$ of 50 μradians with 0.02032 cm (or 0.008″) bevels. The variation from the average σ_{LRCS} caused by the bevels is 0.25%.

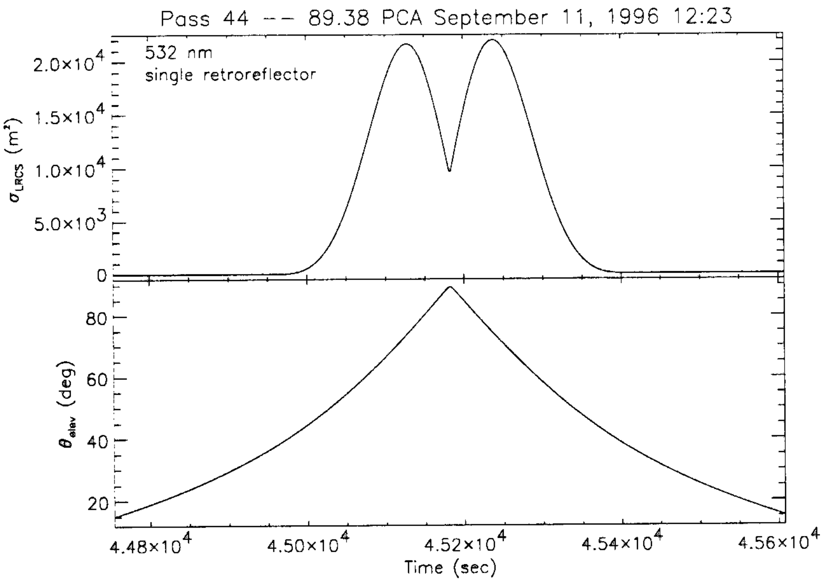

Figure 11: $\sigma_{\rm LRCS}$ of a 1 cm circular retroreflector (top panel) and θ_{elev} (bottom panel) as a function of time during Pass 44. At PCA, $\theta_{elev} = 89.38°$ so this is effectively a zenith pass. Note the impact of retroreflector Field of View (FOV) limit on $\sigma_{\rm LRCS}$.

effect exactly, to first order, the bevels could also be considered as simply a scalar loss of reflecting area combined with a slightly reduced field of view. The combination of both retroreflector tilt and bevel losses requires a slightly more complex numerical simulation, but does not introduce any qualitatively new features to the FFDP or $\sigma_{\rm LRCS}$.

3.2 Single Retroreflector Performance in Orbit

The local geometry at the satellite and apparent velocity for a given ground station must be used to drive the $\sigma_{\rm LRCS}$ routine to compute the performance expected for a single retroreflector on orbit. The range vector, apparent velocity vector, and local elevation angle from nadir are sufficient to determine the k_x, k_y point and what form of $\sigma_{\rm LRCS}$ will occur at a given point in time during a satellite's orbital pass. (See Section A.2 for detailed development.) These two vectors and angle were computed as a function of time for all passes during an ten (9.92) day ground repeat track for Point of Closest Approach (PCA) $\theta_{elev} > 15°$. These passes were provided by NRL Code 8233 for the TOPEX/Poseidon spacecraft over Capraia Island is specified in Section 2.2. The $\sigma_{\rm LRCS}$ values for a single 1 cm nadir-facing retroreflector with 0.008″ bevels are shown in Figure 11 for Pass 44. As can be seen from the figure, the single retroreflector's Field of View (FOV) cutoff (56.7221°) is a dominant constraint; $\sigma_{\rm LRCS}$ is held to zero during those periods in the pass when $\theta_{elev} < 38°$.

The number of detected photons, $N_{\gamma,\rm tele}$, and photoelectrons, $N_{\rm pe}$ for a single 1 cm retroreflector with 0.008″ bevels for Pass 44 are shown in Figures 12 and 13. The performance is evaluated based on both 2 arcsec and 5.4 arcsec pointing uncertainties and 50% receiver path efficiency at 532 nm as discussed in Section 2.2. As can be seen from the Figure 13, detection of 5 photoelectrons may not be possible below θ_{elev} of 57°. Thus, orbital sampling will be severely impacted over the site for a single 1 cm retroreflector.

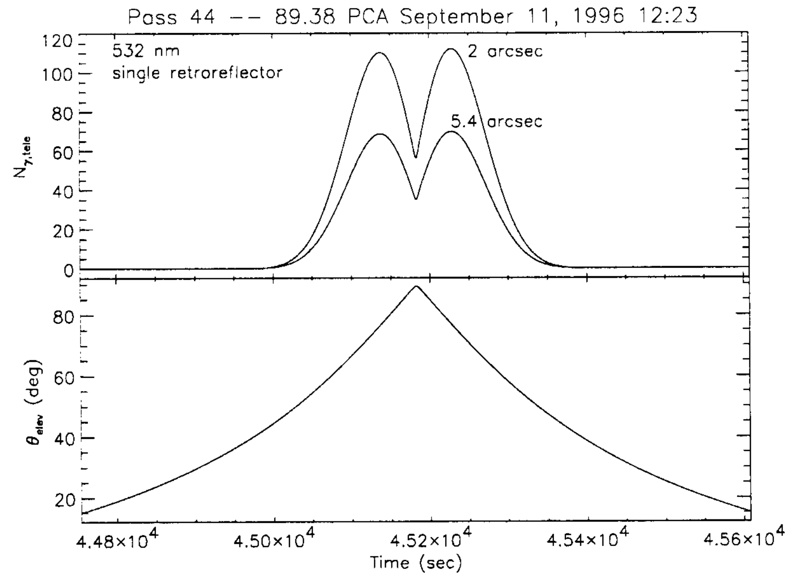

Figure 12: $N_{\gamma,\mathrm{tele}}$ for a 13 cm diameter aperture and 1 cm circular retroreflector as a function of time during Pass 44 assuming either a 2 arcsec or 5.4 arcsec pointing uncertainty.

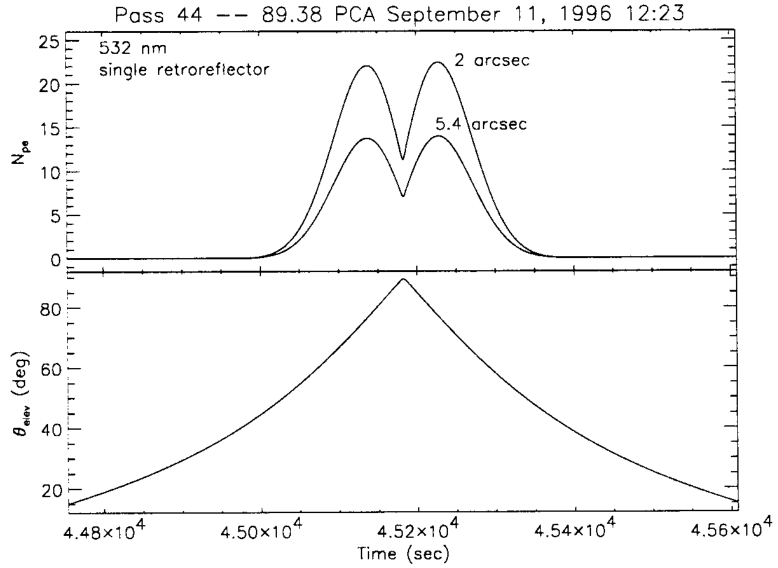

Figure 13: N_{pe} of a 1 cm circular retroreflector as a function of time during Pass 44 assuming either a 2 arcsec or 5.4 arcsec pointing uncertainty.

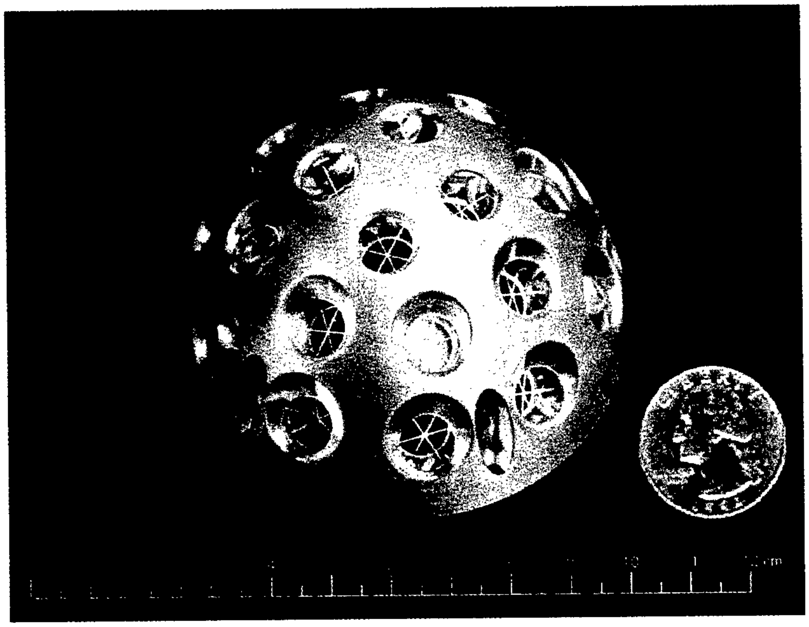

Figure 14: The NRL LEO retroreflector array using 22 individual retroreflectors on the surface of hemisphere. This array has a FOV of 108° and $\sigma_{\mathrm{LRCS}} \geq 10^4$ m^2 for $\theta_{elev} \geq 20°$.

4 RETROREFLECTOR ARRAY DESIGNED FOR LEO

In order to maximize opportunities for ranging and orbital sampling over the site, a retroreflector array can be designed to provide a robust return margin from horizon-to-horizon, if required. The NRL LEO retroreflector array was, in fact, designed to provide a $\sigma_{\mathrm{LRCS}} \geq 10^4$ m^2, through the arc defined by ±20° for a given pass. This array is comprised of 22 1 cm retroreflectors specifically oriented in a hemisphere. The retroreflectors are inset slightly which results in some vignetting (*i.e.* $c \neq 0$ in Equation A-8). A photograph of the array is shown in Figure 14.

The array's multiple retroreflectors are specifically placed to provide a Field-of-View of 108°, yet not impact timing (see Section 4.3). A mechanical drawing of the array is shown in Figure 15. The retroreflectors are in three rings. The first ring is at 16° with four retroreflectors placed at 0°, 90°, 180°, and 270°, in azimuth. The second is at 32° with eight retroreflectors placed at 22.5°, 67.5°, 112.5°, 157.5°, 202.5°, 247.5°, 292.5°, and 337.5° in azimuth. Finally, the third is at 48° with ten retroreflectors placed at 18°, 54°, 90°, 126°, 162°, 198°, 234°, 270°, 306°, and 342° in azimuth.

As with the single retroreflector, far field diffraction effects and velocity aberration must be taken into account to compute predicted performance. However, as will be shown, returns from multiple retroreflectors for a given pulse mitigates nulls in the σ_{LRCS} and permits a much larger FOV.

4.1 σ_{LRCS} of the Retroreflector Array

The return pulse is the sum of the contributions from several retroreflectors in the array. The total FFDP $\tilde{a}$ for the array of L retroreflectors at a given instant of time is

$$\tilde{a} = \sum_{l=1}^{L} \tilde{a}_l e^{i\alpha_l} \quad , \tag{12}$$

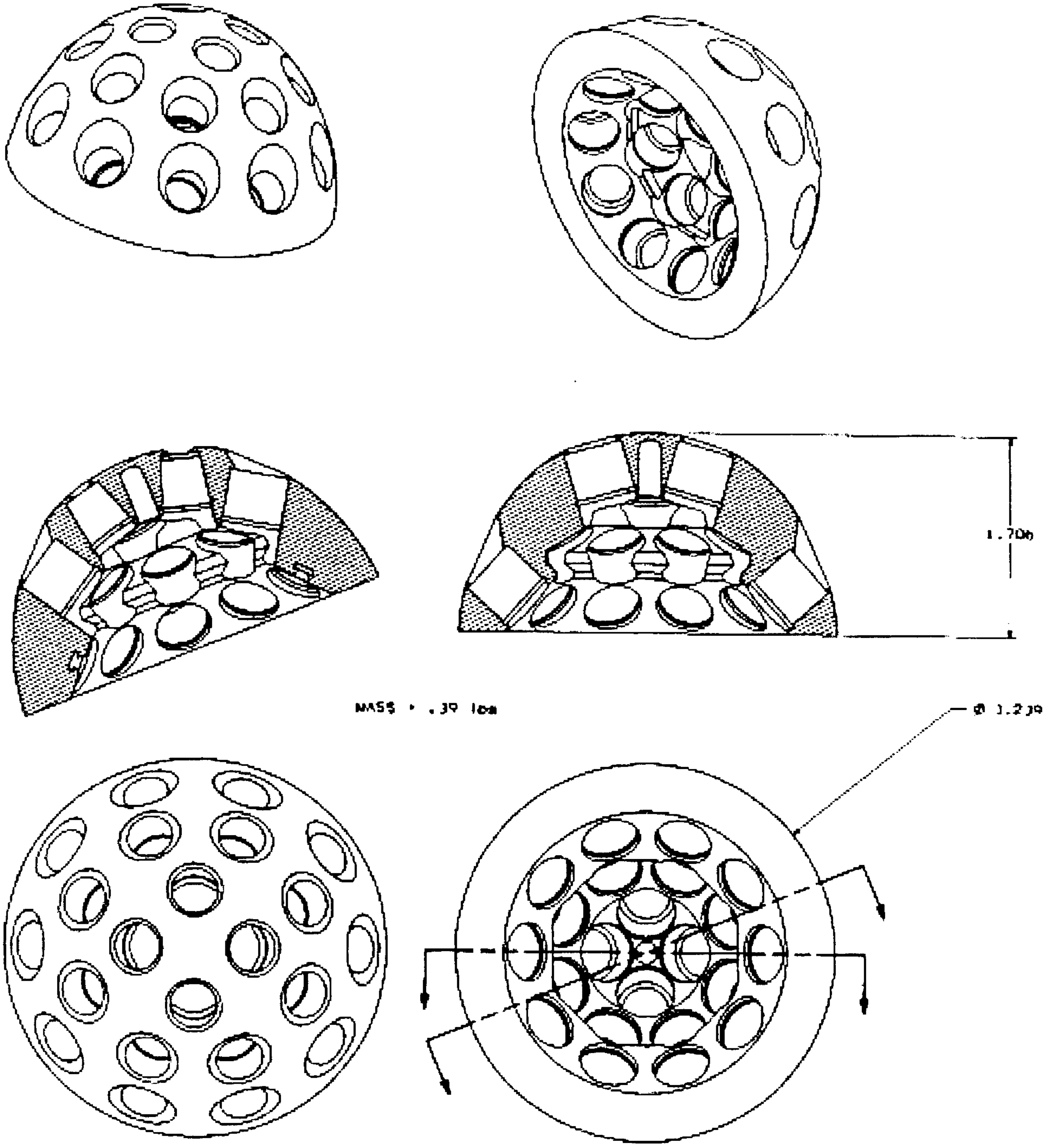

Figure 15: Mechanical Drawings of the NRL LEO Retroreflector Array

where the α_ls are the phase angles for each retroreflector for a given incidence direction. From Equation 8, the instantaneous laser radar cross section is

$$\sigma_{\mathrm{LRCS}} = \rho\frac{4\pi}{\lambda^2}|\tilde{a}\tilde{a}^*| \quad . \tag{13}$$

Upon substitution:

$$\begin{aligned} \sigma_{\mathrm{LRCS}} &= \rho\frac{4\pi}{\lambda^2}\left|\left(\sum_{m=1}^{L}\tilde{a}_m e^{i\alpha_m}\right)\left(\sum_{n=1}^{L}\tilde{a}_n^* e^{-i\alpha_n}\right)\right| & (14)\\ &= \rho\frac{4\pi}{\lambda^2}\left|\sum_{m=1}^{L}\sum_{n=1}^{L}\tilde{a}_m\tilde{a}_n^* e^{i(\alpha_m-\alpha_n)}\right| \quad . & (15)\end{aligned}$$

During the brief interval τ while the laser pulse is reflecting from the array, small variations in orientation will cause essentially random fluctuations among the phase angles for the individual retroreflectors. Consequently, a time-averaged LRCS will simplify to:

$$\begin{aligned} \overline{\sigma_{\mathrm{LRCS}}} &= \rho\frac{4\pi}{\lambda^2}\left|\sum_{m=1}^{L}\sum_{n=1}^{L}\frac{\tilde{a}_m\tilde{a}_n^*}{\tau}\int_0^{\tau} e^{i(\alpha(t)_m-\alpha(t)_n)}dt\right| \quad , & (16)\\ &= \rho\frac{4\pi}{\lambda^2}\sum_{m=1}^{L}|\tilde{a}_m|^2 \quad . & (17)\end{aligned}$$

For SLR measurements with precisions significantly tighter than ±1 cm, τ may be become small enough that the phase integral can not be considered as a Kronecker delta δ_{mn}. For JASON, however, using a random phase approximation is sufficient, and the array's laser radar cross section can be evaluated using the incoherent sum of the contributions in Equation 17.

Equation 17 is a convenient form for numerical evaluation. The routines developed and tested in the single retroreflector can be used directly to compute the $\tilde{a}_m$s. The primary addition is a routine which combines an incidence direction with respect to the array's axis with individual retroreflector directions to determine which retroreflectors are illuminated within their FOV limits and at what angles. It is then straightforward to compute the relevant $\tilde{a}_m$s and to sum to obtain $\overline{\sigma_{\mathrm{LRCS}}}$. Figure 16 shows σ_{LRCS} of the array (using retroreflectors with 0.008″ bevels) as computed numerically when viewed along the array's axis.

4.2 Array Performance in Orbit

As with the single retroreflector, local geometry and velocity aberration combine to determine σ_{LRCS} at any given instant. Similarly, Equation 1 can be used to determine N_{pe} as a function of time during a pass over a given ground site. As in the case of the single retroreflector, the orbital parameters for the TOPEX/Poseidon spacecraft over an ten day ground repeat track over Capraia Island were used to characterize the array's performance. For an array, the local angle from nadir is the angle between the incidence direction and the array's axis. The apparent velocity vector is similarly common to the entire array. As noted in the previous section, this information is first converted into the coordinate system of each illuminated retroreflector in the array and then used to compute σ_{LRCS}.

Figures 17, 18, and 19 show graphs of σ_{LRCS} and θ_{elev} versus time for Pass 44, Pass 85 and a low elevation off-zenith pass respectively. As can be seen from Figures 17 and 18, although there is a drop at nadir, σ_{LRCS} remains greater than 10^4 m^2 throughout the entire pass. By comparison, the response of a single retroreflector (Figure 11) shows vignetting by the FOV and severely limits

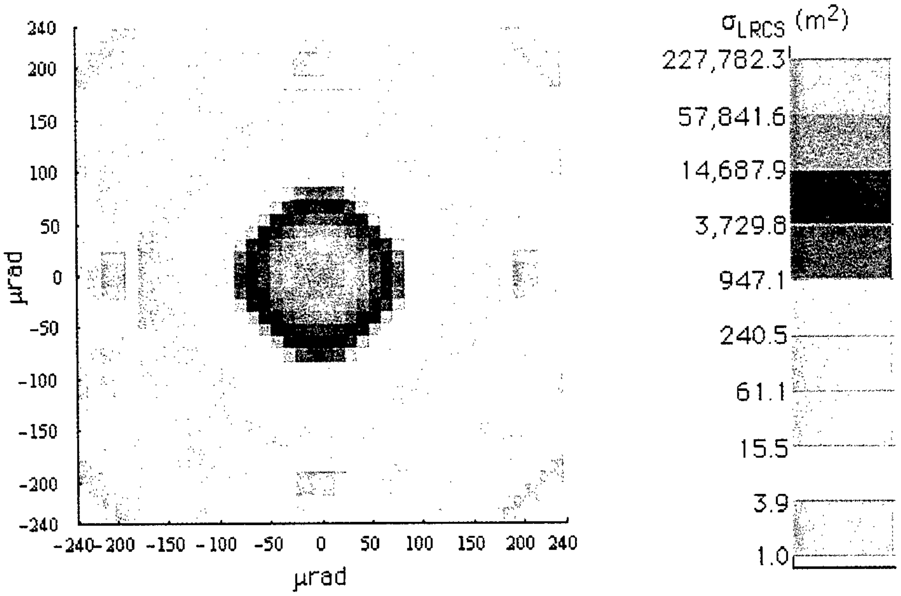

Figure 16: NRL LEO Retroreflector array log(σ_{LRCS}) with 0.008″ bevels and on-axis incidence.

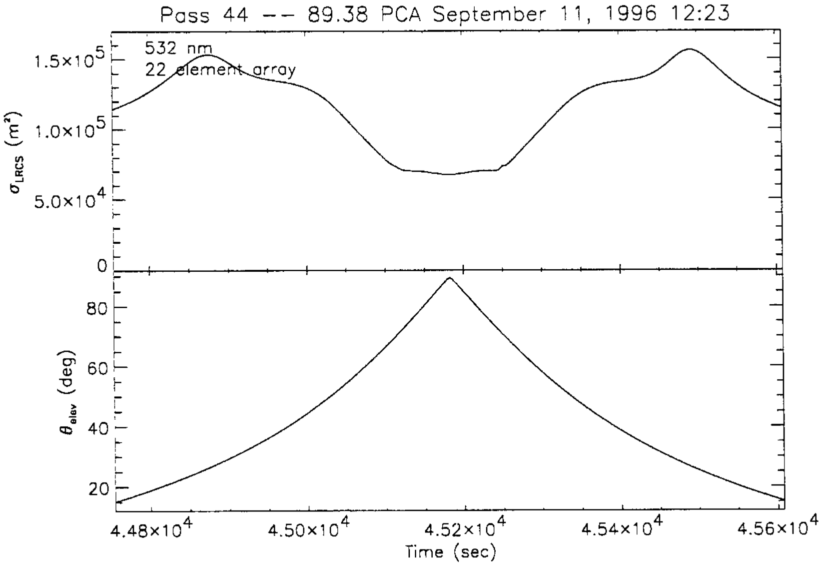

Figure 17: σ_{LRCS} of the 22 element NRL LEO retroreflector array (top panel) and θ_{elev} (bottom panel) as a function of time for Pass 44, at PCA, $\theta_{elev} = 89.38°$.

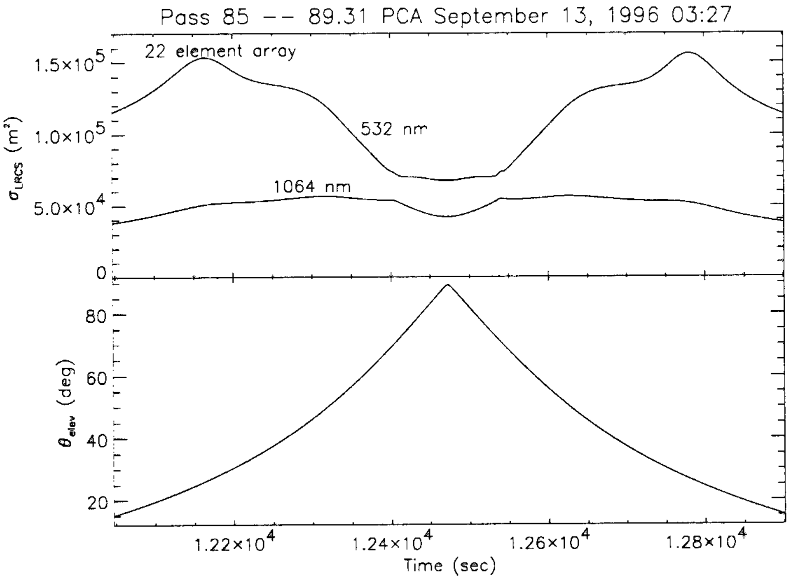

Figure 18: σ_{LRCS} of the 22 element NRL LEO retroreflector array (top panel) and θ_{elev} (bottom panel) as a function of time for Pass 85, at PCA, $\theta_{elev} = 89.31°$.

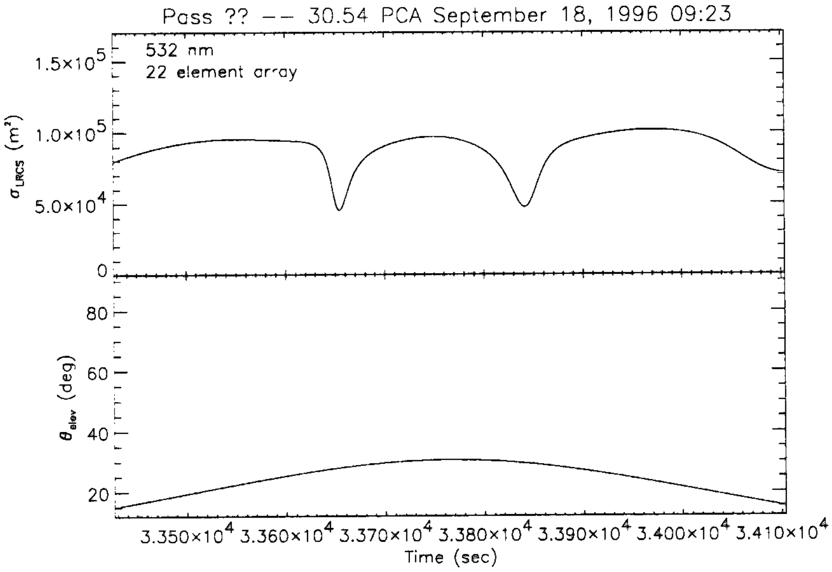

Figure 19: σ_{LRCS} of the 22 element NRL LEO retroreflector array (top panel) and θ_{elev} (bottom panel) as a function of time for a low elevation pass, at PCA, $\theta_{elev} = 30.54°$.

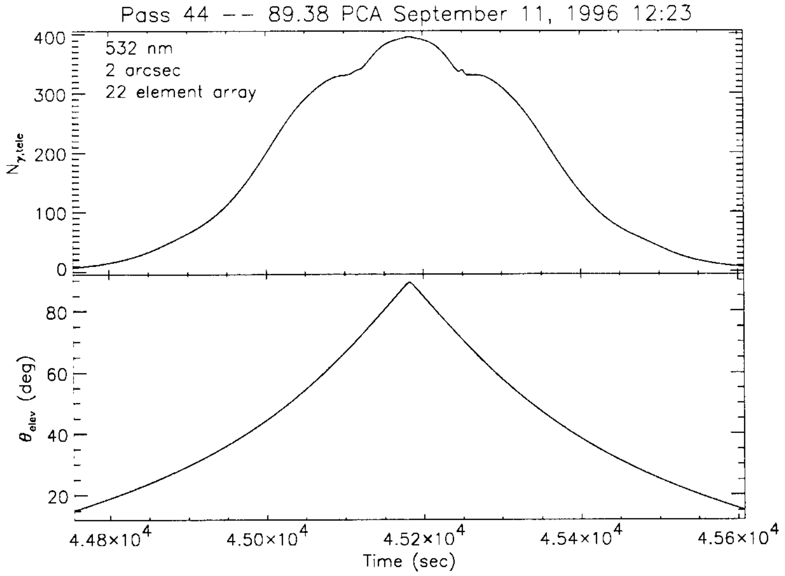

Figure 20: $N_{\gamma,\mathrm{tele}}$ for a 13 cm diameter aperture and the NRL LEO retroreflector array for Pass 44 (top panel) and θ_{elev} (bottom panel) as a function of time during a pass. A pointing precision of 2 arcsec at 532 nm was used in the computations.

viable returns outside a ±57° window. For the low elevation pass, Figure 19 shows $\sigma_{\mathrm{LRCS}} \geq 10^4$ m^2 occurring even at the lowest elevation angles.

Performance on orbit in terms of photon and photoelectron returns are summarized for different parameter sets in Figures 20 through 23. In these computations, we used the MODTRAN atmospheric transmission values shown in Figure 2. For Pass 44, assuming a tracking uncertainty of 2 arcsec, we see from Figures 20 and 21, that we can detect 18 photons and 7 photoelectrons as low as 24.6° elevation at 532 nm. It is of interest to note that for a possibly more realistic pointing accuracy of 5.4 arcsecond, minimum elevation is 28.3° to detect a comparable number of photons and photoelectrons. These results can be seen in Figures 22 and 23.

Performance for Pass 85 was also evaluated. Results were computed for returns at 532 nm and 1064 nm. Photon and photoelectron returns through the pass are shown in Figures 24 and 25. As can be seen in these graphs, the 4% efficiency of the detector at 1064 nm significantly impacts the arc sampled. Predicted returns at 5.4 arcsec pointing uncertainty are shown in Figures 26 and 27.

4.3 Optical Phase Center and Timing Precision

The orbital estimation precision using the SLR data type is on the order of a ±1 cm, RMS. Therefore, knowledge of the offset of the retroreflector's location with respect to the spacecraft Center of Mass (COM) is important. This fixed offset is called the range correction and will exist whether a single retroreflector or an array is used.

In the case of an array, the timing precision of the return signal can also be affected if more than one retroreflector is illuminated by a pulse. The placement of retroreflectors defines an Optical Phase Center (OPC) as the common origin of the all the retroreflector outward normals. To the extent the array retroreflectors lacks a common OPC, a direction-dependent offset will be introduced into the system. Consequently, to achieve centimeter-level precision and accuracy, the retroreflectors

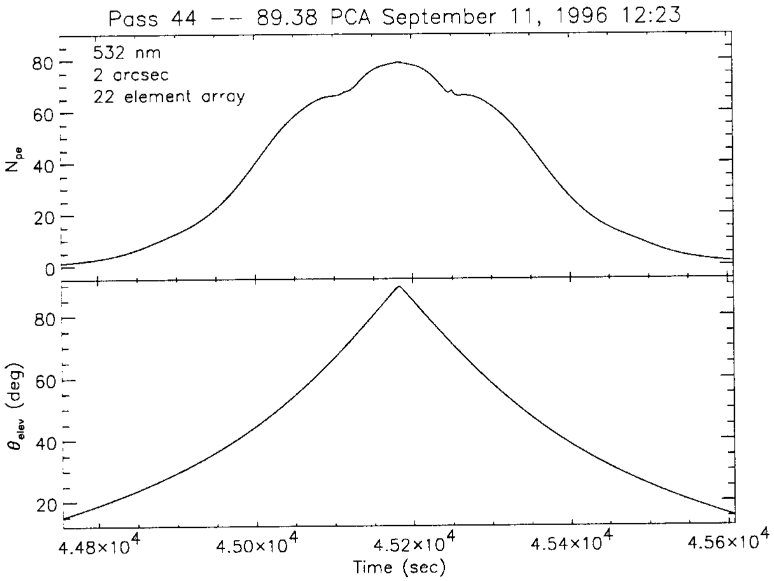

Figure 21: N_{pe} of the NRL LEO retroreflector array for Pass 44 (top panel) and θ_{elev} (bottom panel) as a function of time during a pass. A pointing precision of 2 arcsec at 532 nm was used in the computations.

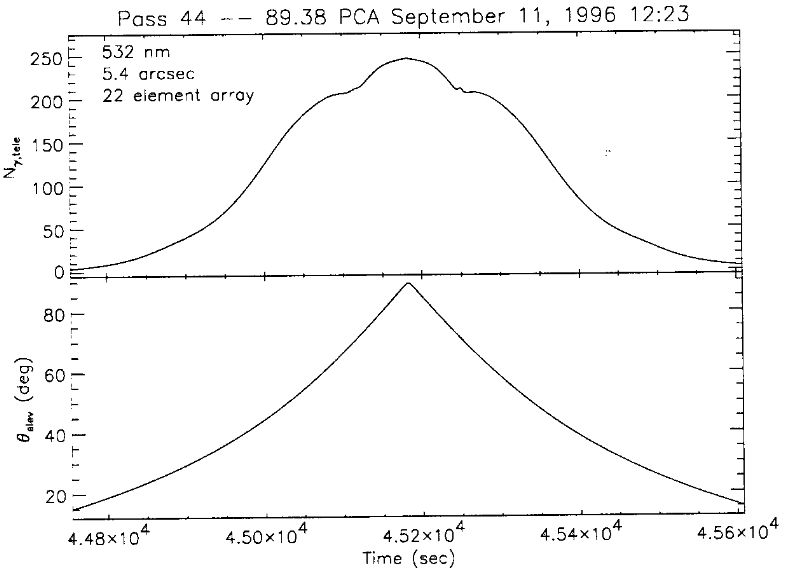

Figure 22: $N_{\gamma,\mathrm{tele}}$ for a 13 cm diameter aperture and the NRL LEO retroreflector array for Pass 44 (top panel) and θ_{elev} (bottom panel) as a function of time during a pass. A pointing precision of 5.4 arcsec at 532 nm was used in the computations.

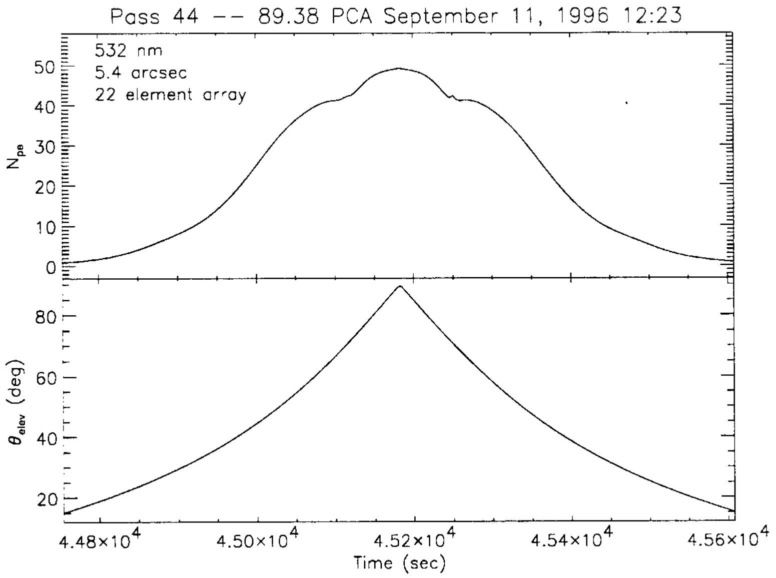

Figure 23: $N_{\rm pe}$ of the NRL LEO retroreflector array for Pass 44 (top panel) and $\theta_{\rm elev}$ (bottom panel) as a function of time during a pass. A pointing precision of 5.4 arcsec at 532 nm was used in the computations.

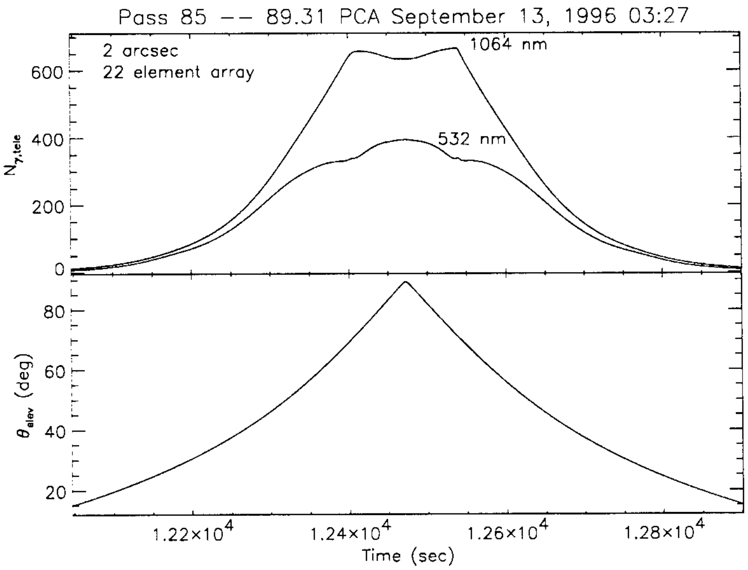

Figure 24: $N_{\gamma,\rm tele}$ for a 13 cm diameter aperture and the NRL LEO retroreflector array for Pass 85 (top panel) and $\theta_{\rm elev}$ (bottom panel) as a function of time during a pass. A pointing precision of 2 arcsec was used in the computations at both 532 nm and 1.064 μm.

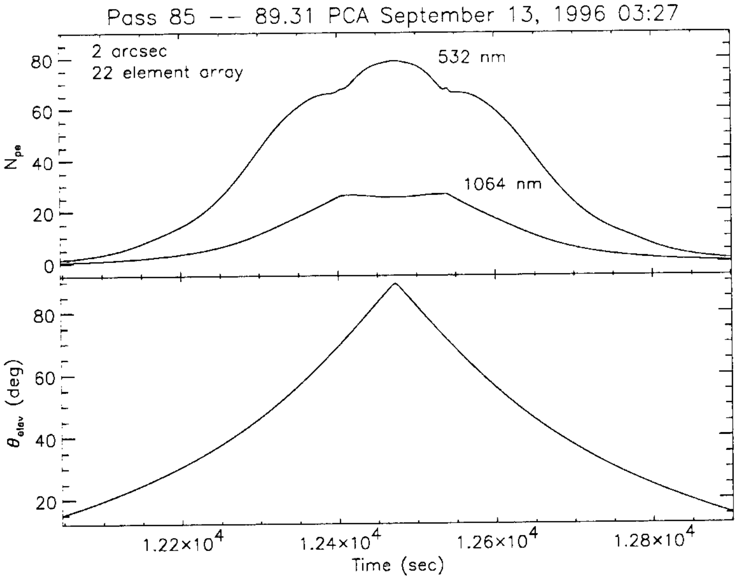

Figure 25: $N_{\rm pe}$ of the NRL LEO retroreflector array for Pass 85 (top panel) and $\theta_{\rm elev}$ (bottom panel) as a function of time during a pass. A pointing precision of 2 arcsec was used in the computations at both 532 nm and 1.064 μm.

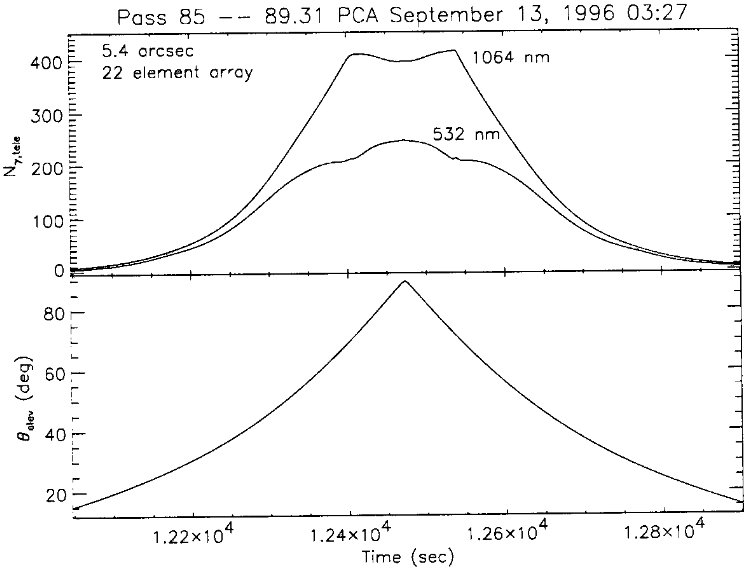

Figure 26: $N_{\gamma,\rm tele}$ for a 13 cm diameter aperture and the NRL LEO retroreflector array for Pass 85 (top panel) and $\theta_{\rm elev}$ (bottom panel) as a function of time during a pass. A pointing precision of 5.4 arcsec was used in the computations at both 532 nm and 1.064 μm.

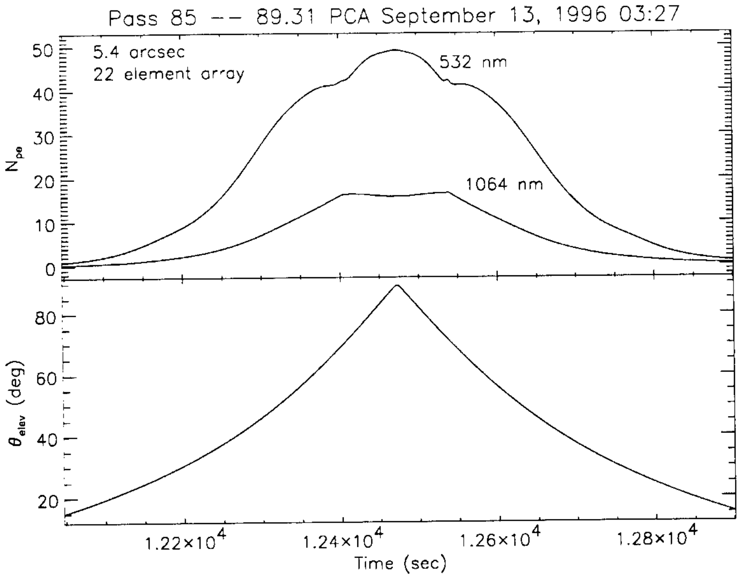

Figure 27: N_{pe} of the NRL LEO retroreflector array for Pass 85 (top panel) and θ_{elev} (bottom panel) as a function of time during a pass. A pointing precision of 5.4 arcsec was used in the computations at both 532 nm and 1.064 μm.

in a multi-element array must be aligned to a comparable tolerance to a common surface.

The OPC of the NRL LEO array is centered on the vertical axis 6 mm inside the array. Centered about this phase center is a surface of reflection. The advantage of a hemisphere of many small reflectors is for any angle there is a retroreflector in close proximity. This condition allows a relatively smooth surface of reflection overall. The radius of this surface was determined by examining 585 angles and calculating the point on this surface for each angle. The surface can be approximated by a sphere with a radius of 2.505 cm. The standard deviation from this sphere is only 0.086 cm. This radius is the largest contributor to the range correction.

The range correction also must consider any pulse broadening due to the multiple retroreflectors. Using small retroreflectors allows for a very compact arrangement. The small size limits the possible pulse broadening. The broadening results from retroreflectors at different locations on the array having a delayed return. For example, using the nadir direction the ring of 4 retroreflectors in the center are closer to the ground then the middle ring of 8 retroreflectors. The time delay is 66 ps. But the return from the middle ring is smaller due to the larger angle. Combing the two returns forms a broaden pulse. The ring of 4 has an average σ_{LRCS} of $52,000$ m^2 and the ring of 8 has an average σ_{LRCS} of only $16,000$ m^2, for nadir. Summing the two returns for an incident pulse of 100 ps FWHM is shown in Figure 28. The pulse is broadened to 117 ps FWHM with a 7 ps (1 mm) delay in the peak amplitude. The extra 17 ps of width contributes to the range error. A 1 mm two way range correction is required to correct for pulse broadening. Longer pulses would have smaller effects.

The range correction error for the time of flight is the combination of the size of the sphere error and the pulse broadening. The increase in the total standard deviation error of the two is ±0.86 mm and ±2.6 mm. Using Gaussian statistics results in a total error of ±2.74 mm. This shows that the array is with in a ± centimeter specification. A more accurate error analysis will require detailed information including the nonlinear behavior of the receiver detector and electronics.

It should be noted that multiple retroreflectors interfere due to the coherence of the laser beam.

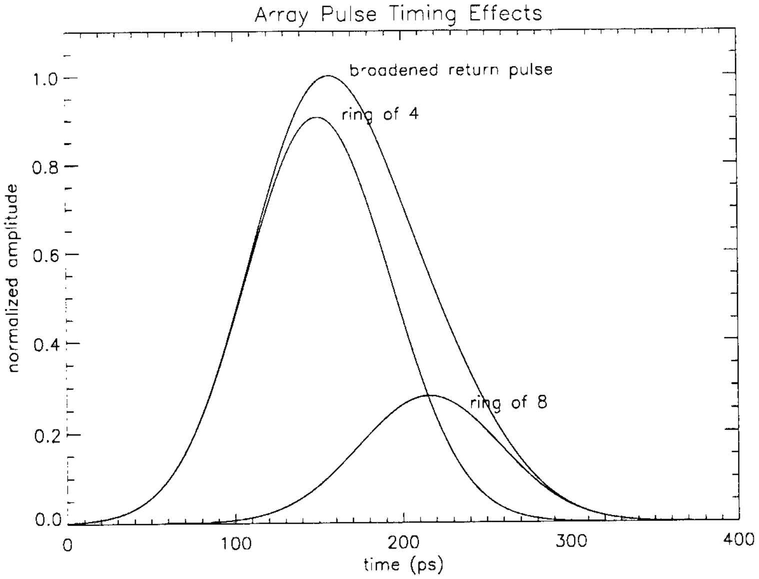

Figure 28: Array Pulse Timing Effects

This effect is termed *satellite scintillation.* An incoherent sum over the array's retroreflectors generates the average return signal, but a coherent sum is required for determining the standard deviation of the return signal. Having more than two retroreflectors in the FOV reduces the deviation. Since the location of each retroreflector at a given moment in time is not known, random phases are assigned to each retroreflector. This is equivalent to moving each retroreflector less than 1μm. This was done analytically for the σ_{LRCS} at each point in the pass and was repeated for 100 random phases for each retroreflector. The resulting standard deviation of the LRCS was less than 12% of the average return signal for all 855 samples of Pass 44. See Figure 29. This deviation is small compared to atmospheric scintillation.

4.4 Further Comparison of Single Retroreflectors and Retroreflector Arrays

Using an array eases the minimum pass geometry requirements significantly. As has been shown, an array can provide viable returns at much lower elevation angles. Using the large set of pass geometries from the ten day repeat cycle as a sample set, the number of passes that exceed a given value of θ_{elev} at PCA as a function θ_{elev} is shown in Figure 30. In other words, Figure 30 shows the number of passes available versus θ_{elev} at PCA. From Figure 11 the single retroreflector σ_{LRCS} places limit of $\theta_{elev} >\sim 40°$. For an array, additional tracking passes can be obtained for a given length of observation time and, consequently a better orbit solution becomes available.

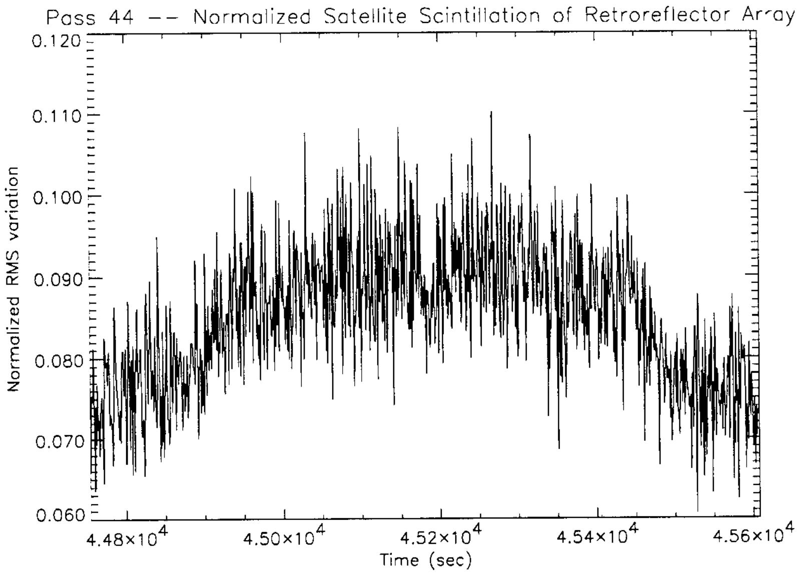

Figure 29: Normalized amplitude fluctuations of the NRL LEO Array. RMS variation in average return signal is 12%.

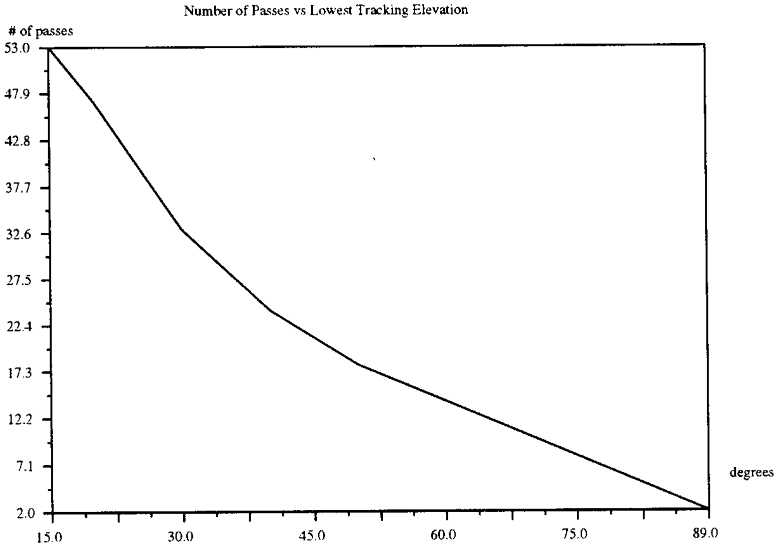

Figure 30: Number of passes versus Lowest Tracking Elevation angle for both the single retroreflector and the array.

5 SPACE QUALIFICATION OF THE NRL LEO RETROREFLECTOR ARRAY

The NRL LEO Retroreflector Array was qualified for space flight with a number of tests. The Qualification Unit is identical to the flight articles except that the optics are slightly flawed. Specifically, the bevels were below the 0.004″ specification on the retroreflectors. The flight qualified retroreflectors were qualified separately by Zygo.

The data taken from the tests described below was analyzed. No thermal-related problems were detected and no negative margins of safety for strength or fatigue were found. A more complete description of the qualification results can be found in Appendix B.

The unit weighs 0.782 ounces, including glass, mount assembly, and bolts for mounting.

5.1 Random Vibration Tests

To conduct the random vibration tests, the unit was mounted on an electrodynamic shaker. The axial and lateral axes were shaken independently. Each vibration was 2 minutes in duration. The axial level was 13.92 G, rms. The lateral level was 13.92 G, rms, as well.

5.2 Thermal Vacuum Tests

The unit was mounted on a thermally-controlled heat sink and thermocouples were used to monitor and control temperature. The vacuum was less than 0.00001 Torr. The unit was tested through 6 cycles from −100° C to 71° C.

5.3 Pyroshock Tests

The unit was mounted on an electrodynamic shaker and again the two axes where shocked independently in axial and lateral dimensions. The peak levels of shock were 6,000 G's.

6 CONCLUSIONS AND CONCERNS

Based on the analysis presented in this report, we predict that JPL and JASON will be able to conduct laser ranging successfully using the NRL LEO array and the FTLRS system at 532 nm, day and night at the TOPEX orbit. However, closing the link in the infrared using the specifications provided, particularly in the daytime, will require photon counting for the small FTLRS aperture. Furthermore, use of this telescope may preclude laser ranging at the lower elevation angles.

REFERENCES

[1] Degnan, John J., "Millimeter Accuracy Satellite Laser Ranging A Review", *Contributions of Space Geodesy to Geodynamics Technology*, **25**, 133–162, 1993.

[2] Gilbreath, G. Charmaine, Mark A. Davis, Peter Rolsma, Richard Eichinger, Timothy Meehan, and John M. Anderson, "Naval Research Laboratory at Starfire Optical Range: Satellite Laser Ranging with Robust Links", SPIE Proceedings, Vol. 3065, 1997 (in press).

[3] Minott, Peter O., "Design of retrodirector arrays for laser ranging of satellites", *NASA TM-X-723-74-122*, Goddard Space Flight Center, 1974.

[4] Minott, Peter O., "Measurement of the lidar cross sections of cube corner arrays for laser ranging of satellites", *NASA TM-X-722-74-301*, Goddard Space Flight Center, 1974.

[5] Born, Max and Emil Wolf, *Principles of Optics*, $6^{\underline{ed}}$, Oxford: Pergamon Press, 395–398, 1985.

[6] Goodman, Joseph W., *Introduction to Fourier Optics*, New York: McGraw-Hill, 61–65, 1968.

A DIFFRACTION PATTERN AND PASS GEOMETRY CALCULATIONS

A.1 Circular Retroreflector Far Field Diffraction Patterns

A convenient method to develop the analytic basis for the numerical determination of far field diffraction pattern begins with the simplest case and then adds refinements. With this approach, numerical implementation of each stage can serve as a limiting test case for the next stage. Our starting case is normal incidence without bevel losses and we will finish with tilted incidence with bevel losses. As has been noted in the body of this report, introducing a tilt in the incidence direction is much larger effect than are the bevel losses.

A.1.1 Normal Incidence Without Bevel Losses

Consider a circular retroreflector with bevel loss regions directly overhead. The two-dimensional Fourier transform of the complex reflectance of the aperture, effectively the retroreflector's far field diffraction pattern, $\tilde{A}(x,y)$ is given by

$$\tilde{a}(k_x,k_y) = \int\int_{\text{aperture}} dxdy\tilde{A}(x,y)\epsilon^{-ik_xx}\epsilon^{-ik_yy} \quad . \tag{A-1}$$

Using the function $c(x)=\sqrt{r^2-x^2}$, which defines the top half of the circular aperture, the double integral can be rewritten as

$$\begin{aligned}
\tilde{a}(k_x,k_y) &= \int_{-r}^{r} dx\epsilon^{-ik_xx}\int_{-c(x)}^{c(x)}\epsilon^{-ik_yy}dy && \text{(A-2)}\\
&= \int_{-r}^{r}\epsilon^{-ik_xx}\frac{1}{-ik_y}\left[\epsilon^{-ik_yc(x)}-\epsilon^{ik_yc(x)}\right]dx && \text{(A-3)}\\
&= \int_{-r}^{r}\epsilon^{-ik_xx}\frac{1}{ik_y}\left[\epsilon^{ik_yc(x)}-\epsilon^{-ik_yc(x)}\right]dx && \text{(A-4)}\\
&= \frac{1}{k_y}\int_{-r}^{r}\epsilon^{-ik_xx}\left[\frac{1}{i}2i\sin k_yc(x)\right]dx && \text{(A-5)}\\
&= \frac{2}{k_y}\int_{-r}^{r}\left[\cos k_xx-i\sin k_xx\right]\sin k_yc(x)dx && \text{(A-6)}\\
&= \frac{2}{k_y}\int_{-r}^{r}\cos k_xx\sin\left(k_y\sqrt{r^2-x^2}\right)dx\\
&\quad -\frac{2i}{k_y}\int_{-r}^{r}\sin k_xx\sin\left(k_y\sqrt{r^2-x^2}\right)dx \quad . && \text{(A-7)}
\end{aligned}$$

When Equation A-7 is integrated numerically, the absolute magnitude of $\tilde{a}(k_x,k_y)$ determined, and then converted to a cross section, the result is the azimuthally symmetric Airy function of Figure 4. The numerical routine that implements this geometry serves as a limit test case for the tilted and normal incidence with bevel losses routines.

A.1.2 Tilted Incidence Without Bevel Losses

When a circular retroreflector is tilted, the aperture changes shape to the overlap region of two offset circles. The tilt away from normal incidence can be related to circles' offset x_0 from the center of the retroreflector. For a retroreflector of depth d with a face recessed by distance c and index of refraction n, the expression relating x_0 to the angle θ_{inci} between the surface normal and the incidence direction is

$$x_0 = c\sin\theta_{inci} + d\sin\theta_n \quad , \tag{A-8}$$

where

$$\theta_n = \arcsin\left(\frac{\sin\theta_{inci}}{n}\right) \quad . \tag{A-9}$$

For a circular retroreflector of radius r, $d = \sqrt{2}r$. The retroreflector's Field Of View (FOV) is limited by the requirement that $x_0 < r$. For a 1 cm diameter retroreflector with $n = 1.46$ and $c = 0.1016$ cm (or $0.040''$), the FOV cut off is at $\theta_{inci} = 58.579°$. The aperture boundary for the tilted retroreflector is defined by $c(x) = \pm\sqrt{r^2 - (x - x_0)^2}$ for $x < 0$ and $c(x) = \pm\sqrt{r^2 - (x + x_0)^2}$ for $x \geq 0$. The aperture's shape is that of a cat's iris or an American football profile shown in the upper panel of Figure 6 (page 9).

Integrating each side of the aperture separately yields a two dimensional Fourier transform for tilted incidence with four integrals given by

$$\begin{aligned}\tilde{a}(k_x, k_y) \quad = \quad & \frac{2}{k_y}\left[\int_{-(r-x_0)}^{0} \cos k_x x \sin\left(k_y\sqrt{r^2 - (x - x_0)^2}\right) dx\right. \\ & \left. + \int_0^{(r-x_0)} \cos k_x x \sin\left(k_y\sqrt{r^2 - (x + x_0)^2}\right) dx\right] \\ & - \frac{2i}{k_y}\left[\int_{-(r-x_0)}^{0} \sin k_x x \sin\left(k_y\sqrt{r^2 - (x - x_0)^2}\right) dx\right. \\ & \left. + \int_0^{(r-x_0)} \sin k_x x \sin\left(k_y\sqrt{r^2 - (x + x_0)^2}\right) dx\right] \quad .\end{aligned} \tag{A-10}$$

Equation A-10 yields reasonable looking transform and limits to an Airy function as $x_0 \to 0$. Figure 8 (page 10) shows the sizable variation in the laser radar cross section of a tilted circular retroreflector as one sweeps k_x and k_y with a constant magnitude of k of 50 μradian (*i.e.* roughly a satellite's velocity aberration for a 1,100 km high orbit).

A.1.3 Normal Incidence With Bevel Losses

Consider a circular retroreflector with bevel loss regions directly overhead. There are six regions, symmetric about the x-axis, that can be used to compute the two-dimensional Fourier transform for the aperture. These regions are shown in Figure 31.

The two-dimensional Fourier transform of the complex reflectance of the aperture $\tilde{A}(x, y)$ is now given by

$$\begin{aligned}&\tilde{a}(k_r, k_y) = \\ &\quad \int_{-r}^{-x_2} dx\epsilon^{-ik_x x} \int_{-c(x)}^{c(x)} \epsilon^{-ik_y y} dy + \int_{-x_2}^{-w} dx\epsilon^{-ik_x x} \int_{l^+(x)}^{-l^+(x)} \epsilon^{-ik_y y} dy \\ &\quad + \int_{-x_1}^{-w/2} dx\epsilon^{-ik_x x}\left[\int_{-c(x)}^{l^-(x)} \epsilon^{-ik_y y} dy + \int_{-l^-(x)}^{c(x)} \epsilon^{-ik_y y} dy\right] \\ &\quad + \int_{w/2}^{x_1} dx\epsilon^{-ik_x x}\left[\int_{-c(x)}^{-l^+(x)} \epsilon^{-ik_y y} dy + \int_{l^+(x)}^{c(x)} \epsilon^{-ik_y y} dy\right] \\ &\quad + \int_{w}^{x_2} dx\epsilon^{-ik_x x} \int_{-l^-(x)}^{l^-(x)} \epsilon^{-ik_y y} dy + \int_{x_2}^{r} dx\epsilon^{-ik_x x} \int_{-c(x)}^{c(x)} \epsilon^{-ik_y y} dy \quad ,\end{aligned} \tag{A-11}$$

where

$$l^+(x) = \frac{1}{\sqrt{3}}(x + w) \tag{A-12}$$

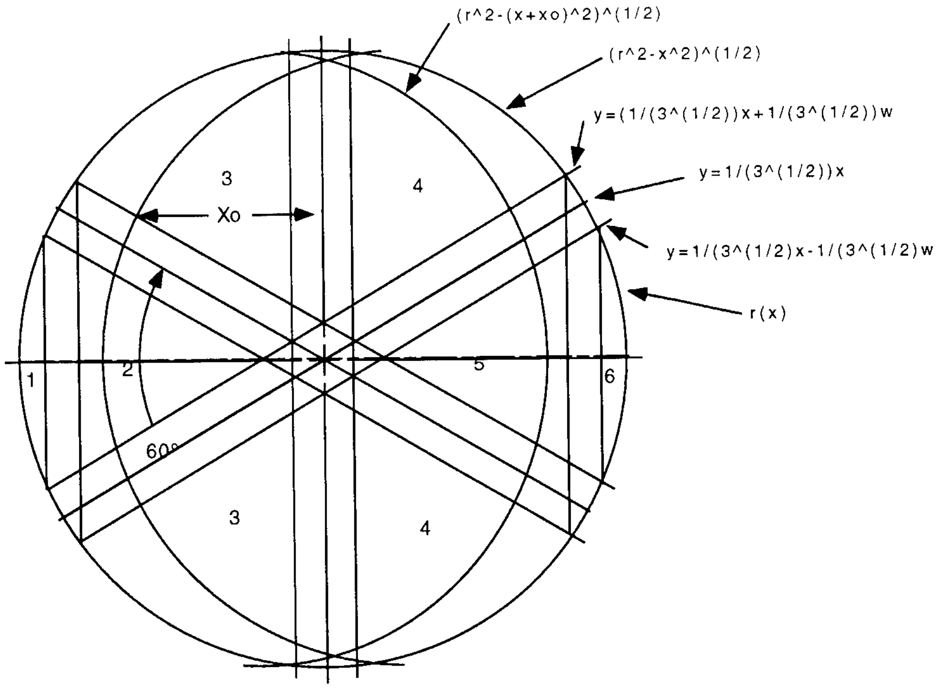

Figure 31: On-axis retroreflector with bevel geometry. The six regions are numbered left to right. Regions 3 and 4 are each made of two pieces.

and

$$l^-(x) = \frac{1}{\sqrt{3}}(x - w) \quad . \tag{A-13}$$

The two integration limits along x determined by the intersection of $l^+(x)$ and $l^-(x)$ and the circular aperture are given by $x_1 = \frac{1}{4}\left(-w + \sqrt{12r^2 - 3w^2}\right)$ and $x_2 = \frac{1}{4}\left(w + \sqrt{12r^2 - 3w^2}\right)$ respectively.

Rather than working with all six terms in Equation A-11 at once, I'll reduce them to forms convenient for numerical integration individually. The six terms are:

$$\tilde{a}_1(k_x, k_y) = \int_{-r}^{-x_2} dx e^{-ik_x x} \int_{-c(x)}^{c(x)} e^{-ik_y y} dy \quad , \tag{A-14}$$

$$\tilde{a}_2(k_x, k_y) = \int_{-x_2}^{-w} dx e^{-ik_x x} \int_{l^+(x)}^{-l^+(x)} e^{-ik_y y} dy \quad , \tag{A-15}$$

$$\tilde{a}_3(k_x, k_y) = \int_{-x_1}^{-w/2} dx e^{-ik_x x} \left[\int_{-c(x)}^{l^-(x)} e^{-ik_y y} dy + \int_{-l^-(x)}^{c(x)} e^{-ik_y y} dy \right] \quad , \tag{A-16}$$

$$\tilde{a}_4(k_x, k_y) = \int_{w/2}^{x_1} dx e^{-ik_x x} \left[\int_{-c(x)}^{-l^+(x)} e^{-ik_y y} dy + \int_{l^+(x)}^{c(x)} e^{-ik_y y} dy \right] \quad , \tag{A-17}$$

$$\tilde{a}_5(k_x, k_y) = \int_{w}^{x_2} dx e^{-ik_x x} \int_{-l^-(x)}^{l^-(x)} e^{-ik_y y} dy \quad , \tag{A-18}$$

and

$$\tilde{a}_6(k_x, k_y) = \int_{x_2}^{r} dx e^{-ik_x x} \int_{-c(x)}^{c(x)} e^{-ik_y y} dy \quad . \tag{A-19}$$

Both $\tilde{a}_1(k_x, k_y)$ and $\tilde{a}_6(k_x, k_y)$ have upper and lower limits of the defined by the circular aperture as in Equation A-2 for the integration along y. Hence, these two terms can be immediately simplified to the same form as Equation A-7 yielding

$$\begin{aligned}\tilde{a}_1(k_x, k_y) &= \frac{2}{k_y}\int_{-r}^{-x_2} \cos k_x x \sin\left(k_y\sqrt{r^2 - x^2}\right) dx \\ &\quad - \frac{2i}{k_y}\int_{-r}^{-x_2} \sin k_x x \sin\left(k_y\sqrt{r^2 - x^2}\right) dx \qquad \text{(A-20)}\end{aligned}$$

and

$$\begin{aligned}\tilde{a}_6(k_x, k_y) &= \frac{2}{k_y}\int_{x_2}^{r} \cos k_x x \sin\left(k_y\sqrt{r^2 - x^2}\right) dx \\ &\quad - \frac{2i}{k_y}\int_{x_2}^{r} \sin k_x x \sin\left(k_y\sqrt{r^2 - x^2}\right) dx \qquad \text{(A-21)}\end{aligned}$$

Note, of course, that the x integration limits in Equations A-20 and A-21 are different than those in Equation A-7. Similarly, $\tilde{a}_2(k_x, k_y)$ and $\tilde{a}_5(k_x, k_y)$ can be reduced to integrals over x of the form

$$\begin{aligned}\tilde{a}_2(k_x, k_y) &= -\frac{2}{k_y}\int_{-x_2}^{-w} \cos k_x x \sin\left(k_y\frac{1}{\sqrt{3}}(x + w)\right) dx \\ &\quad + \frac{2i}{k_y}\int_{-x_2}^{-w} \sin k_x x \sin\left(k_y\frac{1}{\sqrt{3}}(x + w)\right) dx \qquad \text{(A-22)}\end{aligned}$$

and

$$\begin{aligned}\tilde{a}_5(k_x, k_y) &= \frac{2}{k_y}\int_{w}^{x_2} \cos k_x x \sin\left(k_y\frac{1}{\sqrt{3}}(x - w)\right) dx \\ &\quad - \frac{2i}{k_y}\int_{w}^{x_2} \sin k_x x \sin\left(k_y\frac{1}{\sqrt{3}}(x - w)\right) dx \quad . \qquad \text{(A-23)}\end{aligned}$$

Note the sign change of the real and imaginary parts of Equation A-22.

Simplifying $\tilde{a}_3(k_x, k_y)$ and $\tilde{a}_4(k_x, k_y)$ can be done with the same approach. For $\tilde{a}_4(k_x, k_y)$

$$\begin{aligned}&\tilde{a}_4(k_x, k_y) = \\ &\quad \int_{w/2}^{x_1} dx\epsilon^{-ik_x x}\left[\int_{-c(x)}^{-l^+(x)} \epsilon^{-ik_y y} dy + \int_{l^+(x)}^{c(x)} \epsilon^{-ik_y y} dy\right] \qquad \text{(A-24)} \\ &= \int_{w/2}^{x_1} \epsilon^{-ik_x x}\frac{1}{-ik_y}\left[\epsilon^{ik_y l^+(x)} - \epsilon^{ik_y c(x)} + \epsilon^{-ik_y c(x)} - \epsilon^{-ik_y l^+(x)}\right] dx \qquad \text{(A-25)} \\ &= \int_{w/2}^{x_1} \epsilon^{-ik_x x}\frac{1}{ik_y}\left[\epsilon^{ik_y c(x)} - \epsilon^{-ik_y c(x)} - \epsilon^{ik_y l^+(x)} + \epsilon^{-ik_y l^+(x)}\right] dx \qquad \text{(A-26)} \\ &= \frac{1}{k_y}\int_{w/2}^{x_1} \epsilon^{-ik_x x}\left[\frac{1}{i}2i\sin k_y c(x) - \frac{1}{i}2i\sin k_y l^+(x)\right] dx \qquad \text{(A-27)} \\ &= \frac{2}{k_y}\int_{w/2}^{x_1} [\cos k_x x - i\sin k_x x]\sin k_y c(x) dx \\ &\quad - \frac{2}{k_y}\int_{w/2}^{x_1} [\cos k_x x - i\sin k_x x]\sin k_y l^+(x) dx \qquad \text{(A-28)} \\ &= \frac{2}{k_y}\left\{\int_{w/2}^{x_1} \cos k_x x \sin\left(k_y\sqrt{r^2 - x^2}\right) dx\right.\end{aligned}$$

$$
\begin{aligned}
&- \int_{w/2}^{x_1} \cos k_x x \sin\left(k_y \frac{1}{\sqrt{3}}(x+w)\right) dx \Bigg\} \\
&- \frac{2i}{k_y}\left\{ \int_{w/2}^{x_1} \sin k_x x \sin\left(k_y\sqrt{r^2-x^2}\right) dx \right. \\
&\qquad \left. - \int_{w/2}^{x_1} \sin k_x x \sin\left(k_y \frac{1}{\sqrt{3}}(x+w)\right) dx \right\} \quad . \qquad \text{(A-29)}
\end{aligned}
$$

Finally, repeating these steps for $\tilde{a}_3(k_x, k_y)$ yields the similar form

$$
\tilde{a}_3(k_x,k_y) = \int_{-x_1}^{-w/2} dx\epsilon^{-ik_x x}\left[\int_{-c(x)}^{l^-(x)} \epsilon^{-ik_y y} dy + \int_{-l^-(x)}^{c(x)} \epsilon^{-ik_y y} dy\right] \qquad \text{(A-30)}
$$

$$
\begin{aligned}
&= \frac{2}{k_y}\left\{ \int_{-x_1}^{-w/2} \cos k_x x \sin\left(k_y\sqrt{r^2-x^2}\right) dx \right. \\
&\qquad \left. + \int_{-x_1}^{-w/2} \cos k_x x \sin\left(k_y \frac{1}{\sqrt{3}}(x-w)\right) dx \right\} \\
&- \frac{2i}{k_y}\left\{ \int_{-x_1}^{-w/2} \sin k_x x \sin\left(k_y\sqrt{r^2-x^2}\right) dx \right. \\
&\qquad \left. + \int_{-x_1}^{-w/2} \sin k_x x \sin\left(k_y \frac{1}{\sqrt{3}}(x-w)\right) dx \right\} \quad . \qquad \text{(A-31)}
\end{aligned}
$$

The integrals in Equations A-20, A-21, A-22, A-23, A-29, and A-31 are to be evaluated numerically. Figure 10 shows the variation in the σ_{LRCS} of a beveled circular retroreflector as one sweeps k_x and k_y with a constant magnitude of k of 50 μradian (*i.e.* roughly a satellite's velocity aberration). In comparison to the variation seen in Figure 8 (page 10), the bevels do not cause that much change in the magnitude, but do introduce a six-fold symmetry.

A.1.4 Tilted Incidence With Bevel Losses

For a circular retroreflector with bevel loss regions, off-normal incidence angles tilted about the y-axis result in an aperture that is a combination of the cat's eye boundary and bevel loss regions. The position of the bevel loss regions is unchanged and Equation A-8 gives the correct offset in this case as well. Note that the FOV limit now becomes $x_0 < r - \frac{w}{2}$. For a 1 cm diameter retroreflector with $n = 1.46$, $c = 0.1016$ cm (or 0.040″), and $w = 0.01016$ cm (or 0.004″) the FOV cut off is at $\theta_{inci} = 57.63865°$. Since the normal incidence case with bevel losses required distinct integration regions on each side of the aperture, the same six regions used for Equation A-11 can also be used in this case. The two integration limits along x determined by the intersection of $l^+(x)$ and $l^-(x)$ and the aperture change to $x_1 = \frac{3}{4}\left\{-\left(\frac{1}{3}w + x_0\right) + \sqrt{\frac{4}{3}r^2 - \frac{1}{3}(w-x_0)^2}\right\}$ and $x_2 = \frac{3}{4}\left\{\left(\frac{1}{3}w - x_0\right) + \sqrt{\frac{4}{3}r^2 - \frac{1}{3}(w+x_0)^2}\right\}$ respectively. The two dimensional Fourier transform for tilted incidence can be expressed in an analogous form to Equation A-11, where the resulting six terms are given by:

$$
\begin{aligned}
\tilde{a}_1(k_x,k_y) &= \frac{2}{k_y}\int_{-(r-x_0)}^{-x_2} \cos k_x x \sin\left(k_y\sqrt{r^2-(x-x_0)^2}\right) dx \\
&- \frac{2i}{k_y}\int_{-(r-x_0)}^{-x_2} \sin k_x x \sin\left(k_y\sqrt{r^2-(x-x_0)^2}\right) dx \quad , \qquad \text{(A-32)}
\end{aligned}
$$

$$\begin{aligned}
\tilde{a}_2(k_x,k_y) &= -\frac{2}{k_y}\int_{-x_2}^{-w}\cos k_x x\sin\left(k_y\frac{1}{\sqrt{3}}(x+w)\right)dx \\
&\quad+\frac{2i}{k_y}\int_{-x_2}^{-w}\sin k_x x\sin\left(k_y\frac{1}{\sqrt{3}}(x+w)\right)dx \quad , \qquad \text{(A-33)}
\end{aligned}$$

$$\begin{aligned}
\tilde{a}_3(k_x,k_y) &= \frac{2}{k_y}\left\{\int_{-x_1}^{-w/2}\cos k_x x\sin\left(k_y\sqrt{r^2-(x-x_0)^2}\right)dx\right. \\
&\quad\left.+\int_{-x_1}^{-w/2}\cos k_x x\sin\left(k_y\frac{1}{\sqrt{3}}(x-w)\right)dx\right\} \\
&\quad-\frac{2i}{k_y}\left\{\int_{-x_1}^{-w/2}\sin k_x x\sin\left(k_y\sqrt{r^2-(x-x_0)^2}\right)dx\right. \\
&\quad\left.+\int_{-x_1}^{-w/2}\sin k_x x\sin\left(k_y\frac{1}{\sqrt{3}}(x-w)\right)dx\right\} \quad , \qquad \text{(A-34)}
\end{aligned}$$

$$\begin{aligned}
\tilde{a}_4(k_x,k_y) &= \frac{2}{k_y}\left\{\int_{w/2}^{x_1}\cos k_x x\sin\left(k_y\sqrt{r^2-(x+x_0)^2}\right)dx\right. \\
&\quad\left.-\int_{w/2}^{x_1}\cos k_x x\sin\left(k_y\frac{1}{\sqrt{3}}(x+w)\right)dx\right\} \\
&\quad-\frac{2i}{k_y}\left\{\int_{w/2}^{x_1}\sin k_x x\sin\left(k_y\sqrt{r^2-(x+x_0)^2}\right)dx\right. \\
&\quad\left.-\int_{w/2}^{x_1}\sin k_x x\sin\left(k_y\frac{1}{\sqrt{3}}(x+w)\right)dx\right\} \quad , \qquad \text{(A-35)}
\end{aligned}$$

$$\begin{aligned}
\tilde{a}_5(k_x,k_y) &= \frac{2}{k_y}\int_{w}^{x_2}\cos k_x x\sin\left(k_y\frac{1}{\sqrt{3}}(x-w)\right)dx \\
&\quad-\frac{2i}{k_y}\int_{w}^{x_2}\sin k_x x\sin\left(k_y\frac{1}{\sqrt{3}}(x-w)\right)dx \quad , \qquad \text{(A-36)}
\end{aligned}$$

and

$$\begin{aligned}
\tilde{a}_6(k_x,k_y) &= \frac{2}{k_y}\int_{x_2}^{(r-x_0)}\cos k_x x\sin\left(k_y\sqrt{r^2-(x+x_0)^2}\right)dx \\
&\quad-\frac{2i}{k_y}\int_{x_2}^{(r-x_0)}\sin k_x x\sin\left(k_y\sqrt{r^2-(x+x_0)^2}\right)dx \quad . \qquad \text{(A-37)}
\end{aligned}$$

Equations A-32 to A-37 limit properly to the untilted case as $x_0 \to 0$. *(I think.)*

A.2 Converting Pass Geometry to $k_x k_y$ Space

At a given instant the orientation and velocity of the satellite with respect to the ground station determines effective aperture of the retroreflector and the velocity aberration respectively.

For simplicity, consider a nadir pointing retroreflector and use a fixed-earth coordinate system. Hence, the ground station's location vector is a constant denoted by $\vec{\mathbf{G}}$ with fixed spherical coordinates of G, θ_{gs}, and ϕ_{gs}. Note that θ_{gs} is the ground station's colatitude measured down from the north pole rather that the latitude from the equator. The satellite's position is denoted by $\vec{\mathbf{S}}$ with spherical coordinates of S, $\theta_{s/c}$, and $\phi_{s/c}$. The satellite velocity v includes the effect of ground station motion. Finally, the range vector between satellite and ground station is $\vec{\mathbf{R}} = \vec{\mathbf{S}} - \vec{\mathbf{G}}$. Figure 32 illustrates the geometry and the local coordinate system at the satellite.

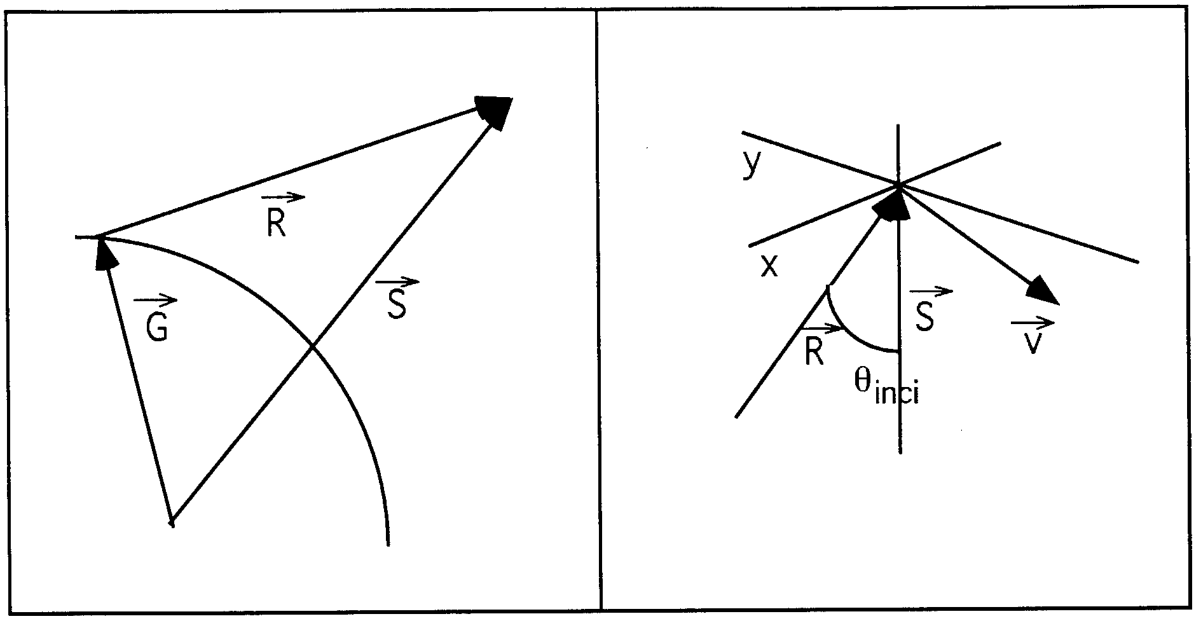

Figure 32: The left panel shows the global definitions of $\vec{\mathbf{G}}$, $\vec{\mathbf{S}}$, and $\vec{\mathbf{R}}$. The right panel shows the coordinate system local to the satellite.

The angle of incidence θ_{inci}, which defines the aperture through Equation A-8, is the angle between $\vec{\mathbf{S}}$, and $\vec{\mathbf{R}}$. Since $\vec{\mathbf{G}}$, $\vec{\mathbf{S}}$, and $\vec{\mathbf{R}}$ form a triangle, θ_{inci} can be related to the angular coordinates of $\vec{\mathbf{G}}$ and $\vec{\mathbf{S}}$ and the elevation angle θ_{elev} of the satellite at the ground site. The angle between $\vec{\mathbf{G}}$ and $\vec{\mathbf{S}}$ is given by

$$\cos\gamma = \cos\theta_{s/c}\cos\theta_{gs} + \sin\theta_{s/c}\sin\theta_{gs}\cos(\phi_{s/c} - \phi_{gs}) \quad . \qquad \text{(A-38)}$$

Hence,

$$\theta_{elev} + \frac{\pi}{2} + \gamma + \theta_{inci} = \pi \qquad \text{(A-39)}$$

or

$$\theta_{elev} + \gamma + \theta_{inci} = \frac{\pi}{2} \quad . \qquad \text{(A-40)}$$

In practice, the values of θ_{inci} and θ_{elev} as a function of time during the pass are computed directly by orbital dynamics software. When working with a retroreflector array, θ_{inci} is the angle between $\vec{\mathbf{R}}$ and the array's axis. Hence, one must do a little further computation to determine the angle of incident for each retroreflector with respect to $\vec{\mathbf{R}}$.

The apparent velocity of the retroreflector can be expressed in terms of the velocity, the ground station position and satellite position. Once the velocity components in a satellite local coordinate system are determined, the values of k_x and k_y that defined the ground stations position in the far field diffraction pattern can be obtained immediately. The local coordinate system with $\hat{x}$ in the plane defined by $\vec{\mathbf{S}}$, and $\vec{\mathbf{R}}$

$$\hat{z} = -\hat{\mathbf{S}} \quad , \qquad \text{(A-41)}$$

$$\hat{y} = \frac{\vec{\mathbf{R}} \times \vec{\mathbf{S}}}{|\vec{\mathbf{R}} \times \vec{\mathbf{S}}|} \quad , \qquad \text{(A-42)}$$

and

$$\hat{x} = \hat{y} \times \hat{z} \quad . \qquad \text{(A-43)}$$

Hence

$$\begin{aligned} v_y &= \frac{\vec{\mathbf{R}} \times \vec{\mathbf{S}}}{|\vec{\mathbf{R}} \times \vec{\mathbf{S}}|} \cdot \vec{\mathbf{v}} \quad , & \text{(A-44)} \\ &= \frac{(\vec{\mathbf{S}} - \vec{\mathbf{G}}) \times \vec{\mathbf{S}}}{|(\vec{\mathbf{S}} - \vec{\mathbf{G}}) \times \vec{\mathbf{S}}|} \cdot \vec{\mathbf{v}} \quad , & \text{(A-45)} \\ &= \frac{\vec{\mathbf{S}} \times \vec{\mathbf{G}}}{|\vec{\mathbf{S}} \times \vec{\mathbf{G}}|} \cdot \vec{\mathbf{v}} \quad . & \text{(A-46)} \end{aligned}$$

Similarly

$$\begin{aligned} v_x &= \frac{\vec{\mathbf{R}} \times \vec{\mathbf{S}}}{|\vec{\mathbf{R}} \times \vec{\mathbf{S}}|} \times -\hat{\mathbf{S}} \cdot \vec{\mathbf{v}} \quad , & \text{(A-47)} \\ &= \frac{\left[(\vec{\mathbf{S}} - \vec{\mathbf{G}}) \times \vec{\mathbf{S}}\right]}{|(\vec{\mathbf{S}} - \vec{\mathbf{G}}) \times \vec{\mathbf{S}}|} \times -\hat{\mathbf{S}} \cdot \vec{\mathbf{v}} \quad , & \text{(A-48)} \\ &= \frac{\hat{\mathbf{S}} \times \vec{\mathbf{S}} \times \vec{\mathbf{G}}}{|\vec{\mathbf{S}} \times \vec{\mathbf{G}}|} \cdot \vec{\mathbf{v}} \quad . & \text{(A-49)} \end{aligned}$$

Finally,

$$k_x = \left(\frac{2\pi}{\lambda}\right)\left(\frac{2v_x}{c}\right) \tag{A-50}$$

and

$$k_y = \left(\frac{2\pi}{\lambda}\right)\left(\frac{2v_y}{c}\right) \quad . \tag{A-51}$$

The numerical routine to determine k_x and k_y from the results provided by the orbital dynamics group is a distinct module to simplify testing.

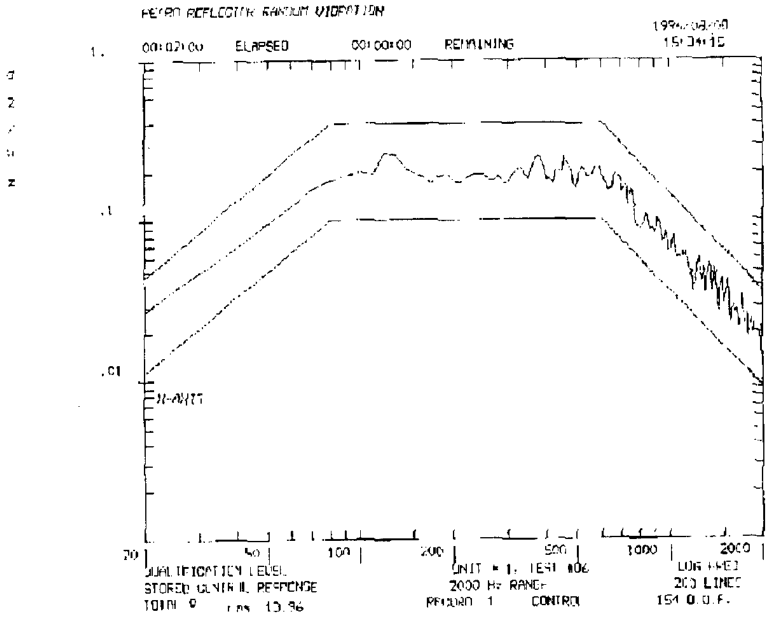

Figure 33: Lateral Accelerometer Data

B CODE 8200 SPACE QUALIFICATION REPORT

B.1 Test Report For The Retro-Reflector Array

August 1996
Robert B. Patterson
U.S. Naval Research Laboratory

B.1.1 Random Vibration Tests

The test article (RR-ST-1100-01 assembly) was subjected to two random vibration tests. One in the axial (Z-axis) direction and one in the lateral (X-axis) direction. Since the assembly is a symmetrical round dome, a test in the Y-axis direction was considered unnecessary.

The test article was assembled using flight quality parts with the exception of the optics, which are identical to the flight quality units in all physical characteristics, but have slight flaws in the optical properties. The qualification dome (RR-ST-1030-1) was not irradiated, this will have no effect on the fit of the parts to one another or the strength or stiffness of that part or the assembly.

The lateral test was run first. The accelerometer data, from an accelerometer mounted on the shake table close to the test article, is shown in Figure 33. The test article survived the random vibration test in the lateral axis.

The axial test was run next. The accelerometer data is shown in Figure 34. The test article survived the random vibration test in the axial axis.

B.1.2 Shock Testing

The shock tests were next. Again only an axial and lateral test were needed. The test was performed on the same shake table that was used to perform the random vibration tests. The accelerometer data was obtained the same way, with the accelerometer mounted on the test fixture close to the test article.

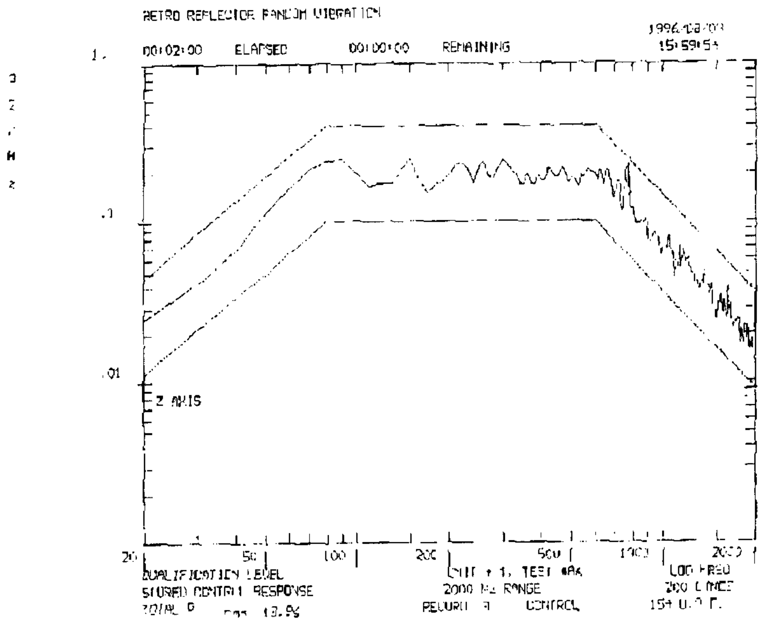

Figure 34: Axial Accelerometer Data

The axial shock test was completed first. The test article passed. The accelerometer data is shown in Figure 35.

The lateral shock test was then run. The test article passed. The accelerometer data is shown in Figure 36

B.1.3 Thermal Vacuum Testing

The qualification assembly was placed in a small vacuum chamber and cycled between the survival temperature extremes to verify that the assembly could survive the environments it will see while attached to the host. This was done by bolting the assembly to a small "cold" plate that had its temperature controlled by allowing liquid nitrogen to flow through copper tubing that was soldered to the backside of the copper "cold" plate or by applying power to electrical heaters that are attached to the front side of the plate, or some combination of the two. The plate had two thermocouples mounted to it. One was for feedback to the controller used to control the flow of liquid nitrogen and the other was used as the data for the test.

The test article was placed in the vacuum chamber, which was then pumped down to a vacuum of at least 0.0001 torr. The assembly was then subjected to temperature extremes of 71° C for the high temperature and −100° C for the low temperature. The assembly was held at each temperature extreme for a one hour dwell period to insure that the test article stabilized at the test temperature. The test consisted of 6 cold dwells alternated with 6 hot dwells.

The qualification assembly passed the test without suffering any failures. The test went according to plan, except when the control valve stuck open and the temperature went down to −157° C during the second cold dwell. Since the temperature stayed below the maximum of −100° C, this did not negate this part of the test. The faulty valve was changed out during the next transition from cold to hot dwell and the test continued. A time versus temperature graph of the test profile is shown in Figure 37.

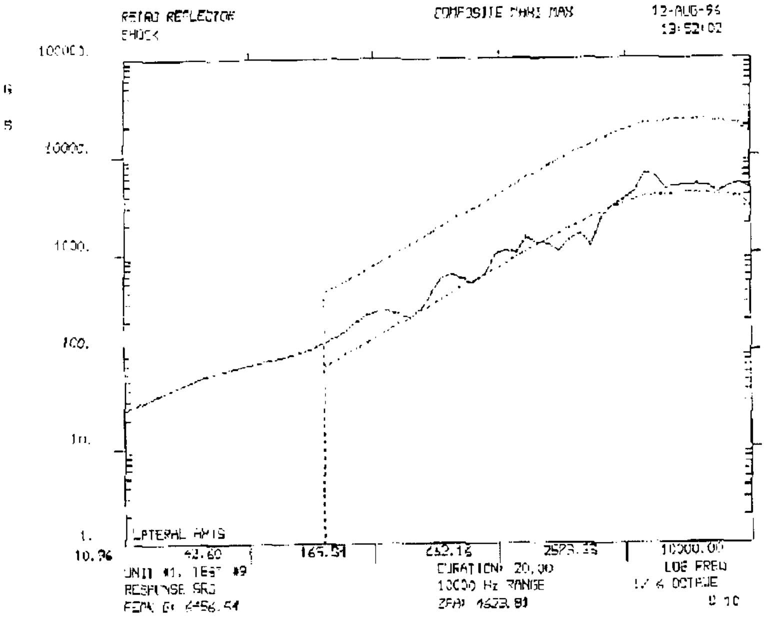

Figure 35: Axial Shock Accelerometer Data

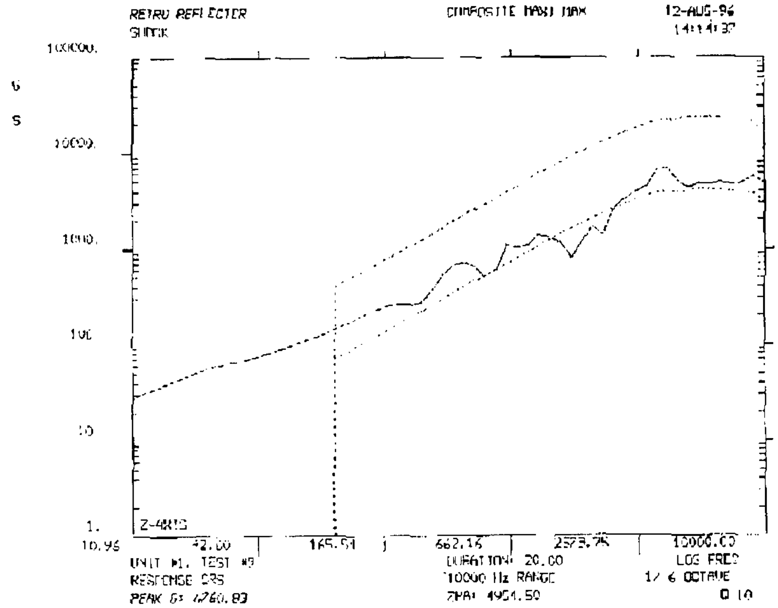

Figure 36: Lateral Shock Accelerometer Data

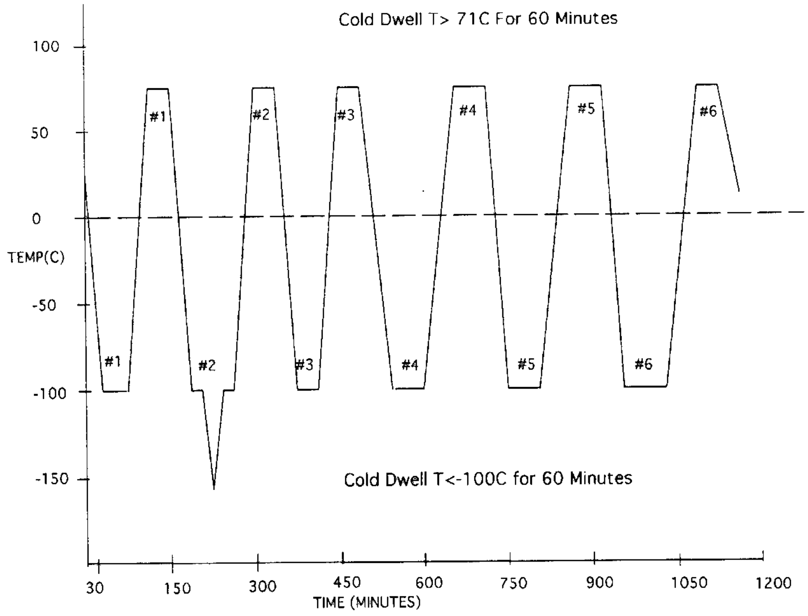

Figure 37: Thermal Vacuum Test Temperature Profile

B.2 Test Procedure For The Retro-Reflector Array

June 19, 1996
Robert B. Patterson
U.S. Naval Research Laboratory

B.2.1 Test Definition

B.2.1.1 Scope This document contains the requirements and procedures for the random vibration, shock and thermal testing to be performed on the retroreflector array in order to qualify it for space flight on its host.

B.2.1.2 Test Objective The objective of this testing is to insure that the retroreflector array is structurally sound and can withstand the launch and post launch environments without experiencing any structural failure.

B.2.1.3 Pass/Fail Criteria

1. No parts (spring, retaining ring, retro seat or retro optic) ejected from the assembly.
2. No noticeable permanent deformation around the seat area at the optic opening in the retroreflector housing.
3. No noticeable permanent deformation around the retaining ring groove area of the retroreflector housing.

B.2.1.4 Test Description Since the retro-reflector assembly is a round part that is symmetrical about the axis of rotation, we will only have to test it in one longitudinal direction and the axial direction. We will mount the retro-reflector assembly to the shaker table so that it is oriented to be tested in the longitudinal direction. We will then run the test article through the 13.92 Grms

Random Vibration test environment. We will then "hit" the test article with an extremely sharp impulse in order to simulate the shock environment (6000 g) specified by the host vehicle. We will now remount the retro-reflector assembly so that it is oriented in the axial direction and repeat the random vibration and shock tests.

The thermal test consists of bolting the retro-reflector assembly to a "cold" plate (that also has heaters installed on it), placing this assembly into a vacuum chamber and then cycling the assembly through its survival temperature extremes six times.

B.2.1.5 Test Location The test will be conducted in the Naval Center for Space Technology's Payload Checkout Facility, Building A-59 at the Naval Research Laboratory in Washington, DC.

B.2.1.6 Responsibilities The Spacecraft Engineering Department is responsible for the overall performance of the test, the data reduction, and production of the final test report.

B.2.1.7 Test Log The test conductor shall maintain a daily test log which shall include a detailed record of the test progress, significant events and any deviations from the test procedures outlined in this document.

B.2.1.8 Photographic Coverage Photographs will be taken of the test specimens, test fixtures and peripheral test equipment. Each transducer location will be marked and photographed.

B.2.2 Test Conditions

B.2.2.1 General The test will be conducted in the ambient temperature and pressure in the Payload Checkout Facility, Building A-59, Naval Research Laboratory.

B.2.2.2 Applied Loads The test articles shall be tested to the levels described by the host vehicle as listed in NCST Qual. Procedures, Appendix A. The qualification unit shall be tested to qualification levels and the flight unit shall be tested to acceptance levels.

B.2.2.3 Test Report A final test report will be prepared to document the test results. This report shall include overall test objectives, test article and test setup descriptions, reduced test data, test anomalies and/or significant observations and a summary of the test results.

B.3 Final Acceptance Test Report Of The Retro-Reflector Array

November 1996
Robert B. Patterson
U.S. Naval Research Laboratory

B.3.1 Random Vibration Tests

The flight units (RR-ST-1100-01 assembly) were subjected to two random vibration tests each. One in the radial (Z-axis) direction and one in the lateral (X-axis) direction. Since the assembly is a symmetrical round dome, a test in the Y-axis direction was considered unnecessary.

The flight units were assembled using flight quality parts and were labeled assembly A, B, and C. The flight units were tested to acceptance (flight) levels 6 dB below qualification for a total of 6.92 GRMS.

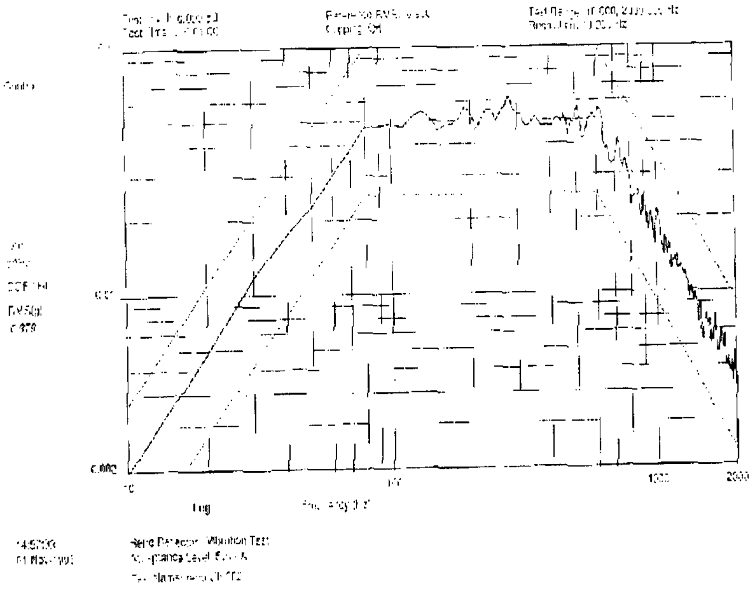

Figure 38: Lateral Accelerometer Data, Acceptance Level S/n -A

The lateral test was run first. The accelerometer data, from an accelerometer mounted on the shake table close to the test article, is shown in Figures 38, 39, and 40. The flight units survived the random vibration test in the lateral axis.

The axial tests were run next. The accelerometer data is shown in Figures 41, 42, and 43. The flight units survived the random vibration test in the axial axis.

B.3.2 Shock Testing

The shock tests were next. Again only an axial and lateral test were needed. The test was performed on the same shake table that was used to perform the random vibration tests. The accelerometer data was obtained the same way, with the accelerometer mounted on the test fixture close to the test article.

The axial shock test was completed first. The flight units passed. The accelerometer data is shown in Figures 44, 45, and 46.

The lateral shock test was then run. The flight units passed. The accelerometer data is Figures 47, 48, and 49.

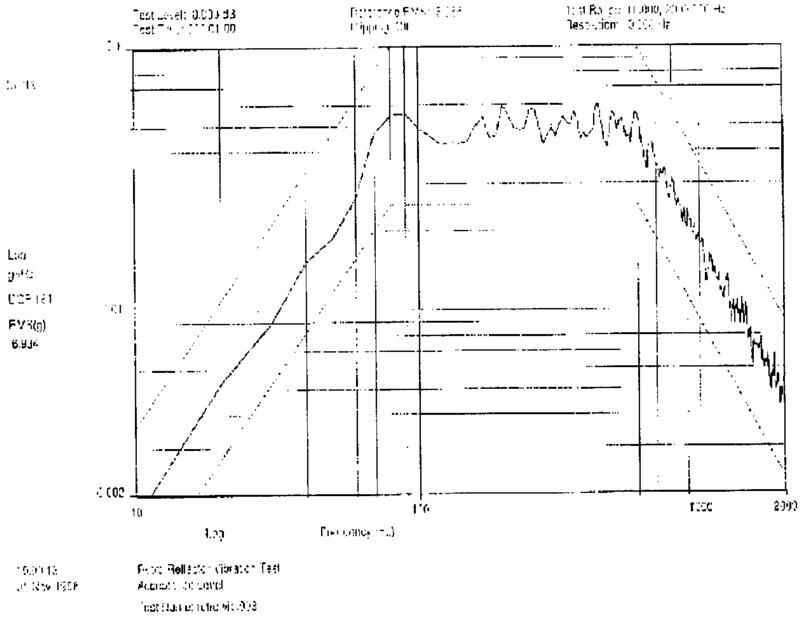

Figure 39: Lateral Accelerometer Data, Acceptance Level S/n -B

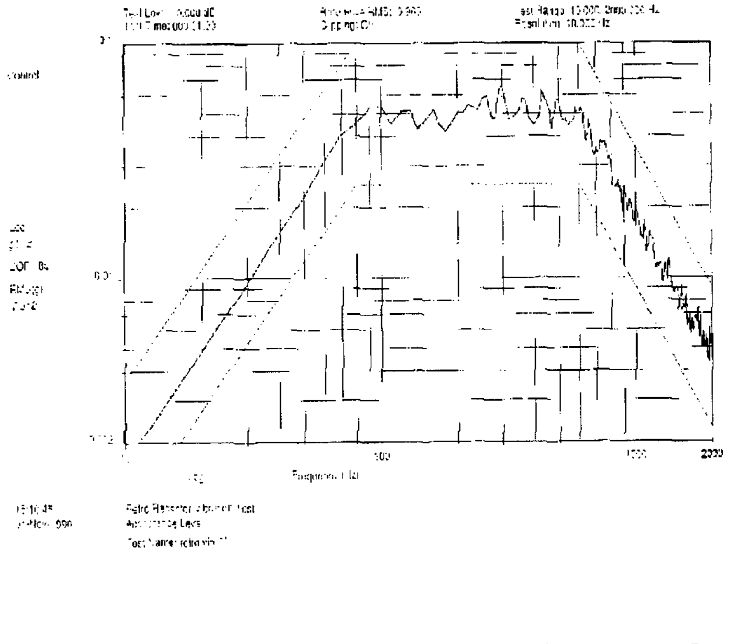

Figure 40: Lateral Accelerometer Data, Acceptance Level S/n -C

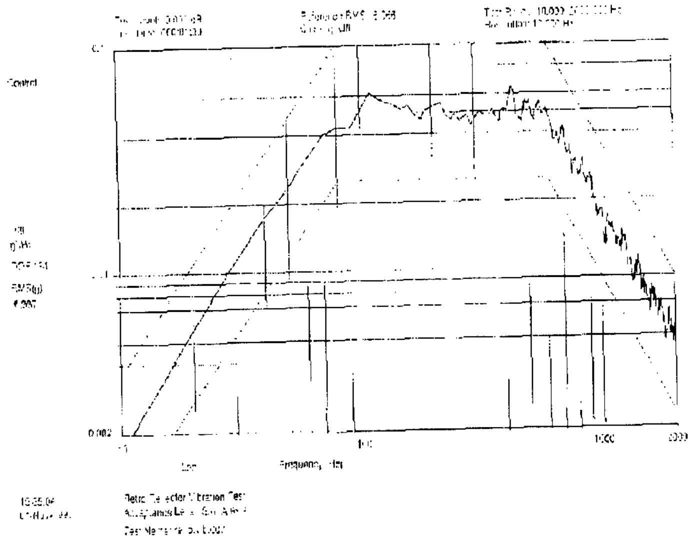

Figure 41: Axial Accelerometer Data, Acceptance Level S/n -A

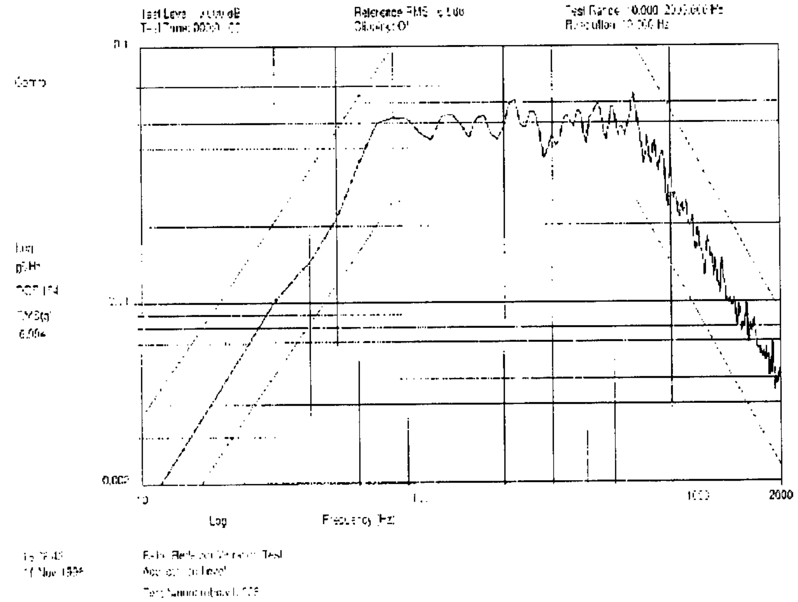

Figure 42: Axial Accelerometer Data, Acceptance Level S/n -B

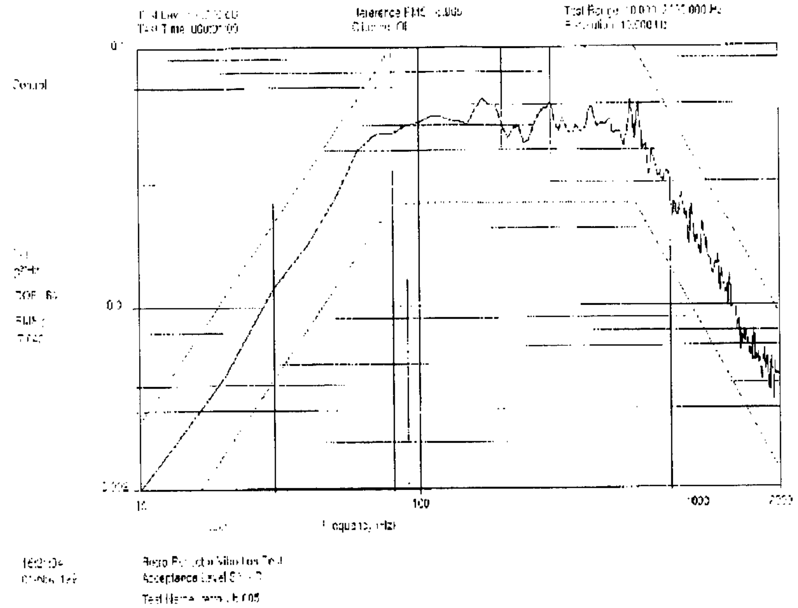

Figure 43: Axial Accelerometer Data, Acceptance Level S/n -C

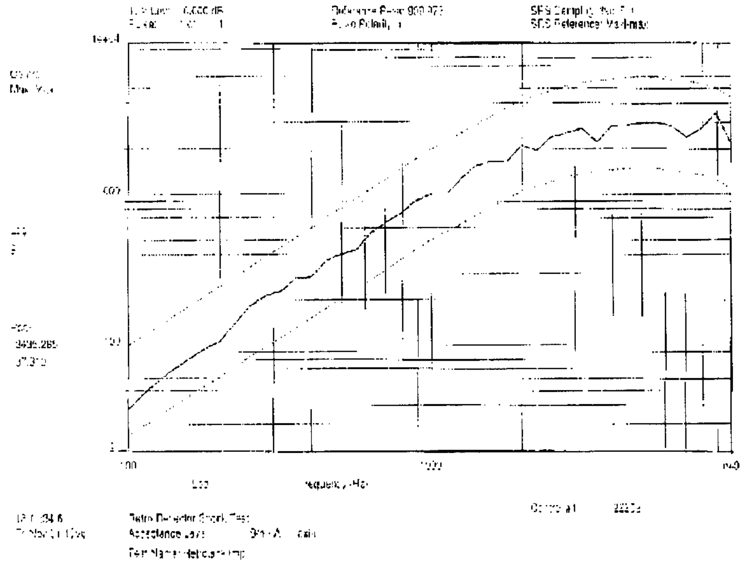

Figure 44: Axial Shock Accelerometer Data, Acceptance Level S/n - A

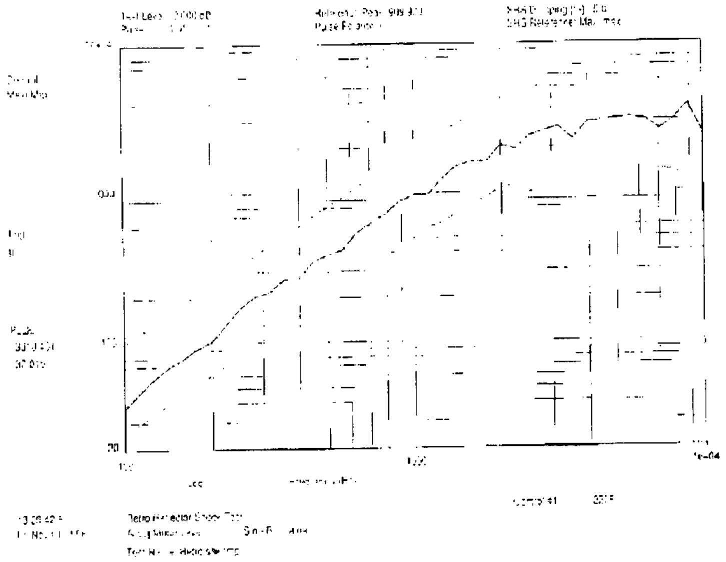

Figure 45: Axial Shock Accelerometer Data, Acceptance Level S/n - B

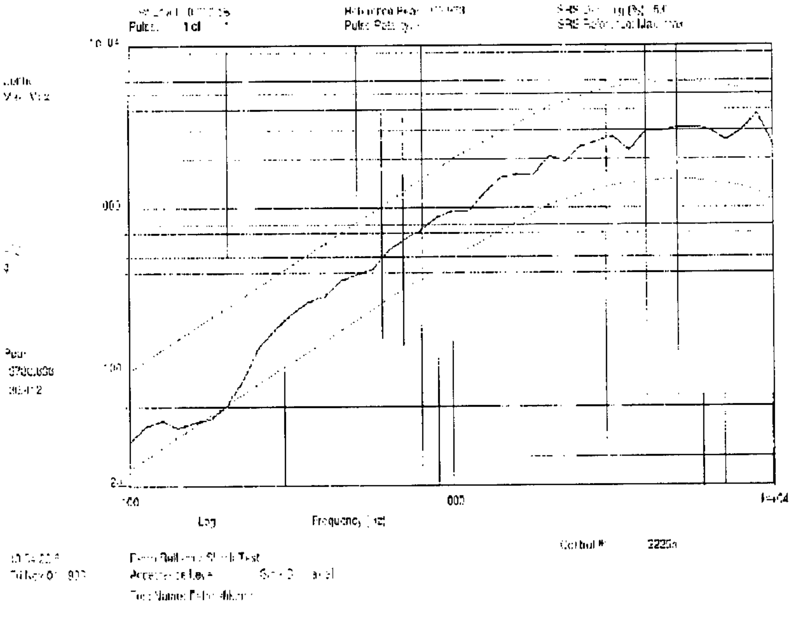

Figure 46: Axial Shock Accelerometer Data, Acceptance Level S/n - C

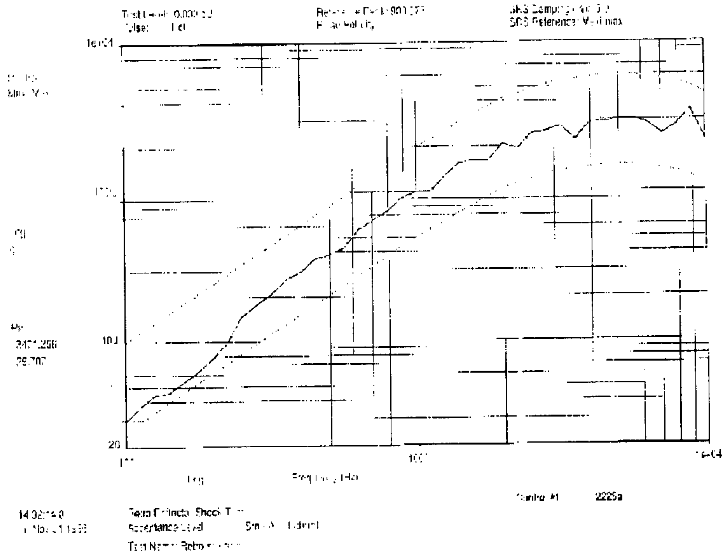

Figure 47: Lateral Shock Accelerometer Data, Acceptance Level S/n - A

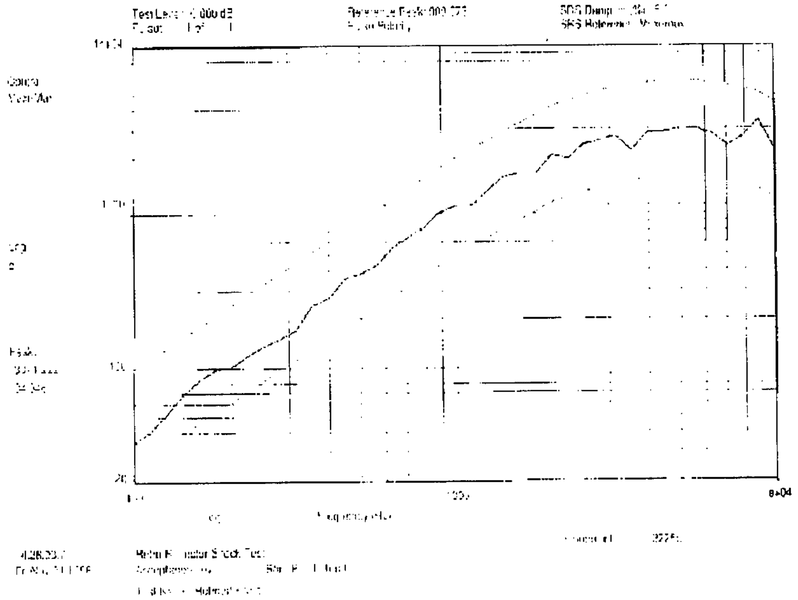

Figure 48: Lateral Shock Accelerometer Data, Acceptance Level S/n - B

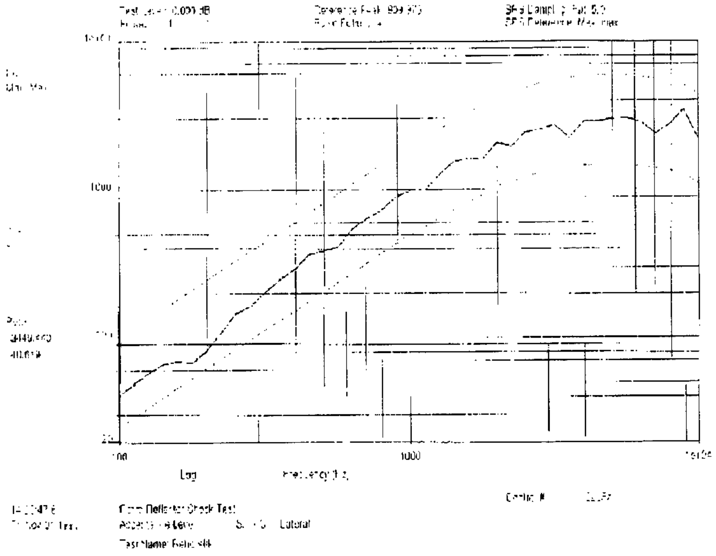

Figure 49: Lateral Shock Accelerometer Data, Acceptance Level S/n - C

C ACRONYM LIST

APD Avalanche PhotoDiode

COM Center of Mass

FFDP Far Field Diffraction Pattern

FOD Field of Dreams

FOV Field of View

FTLRS Field Transportable Laser Radar Station

FWHM Full Width at Half Maximum

JPL Jet Propulsion Laboratory

LEO Low Earth Orbit

LRCS Laser Radar Cross-Section (or σ_{LRSC})

MOBLAS MOBile LAser ranging System

OPC Optical Phase Center

PCA Point of Closest Approach

SLR Satellite Laser Ranging

SOR Starfire Optical Range

TLRS Transportable Laser Ranging System